# HYDRODYNAMIC SIMULATION OF THE COSMOLOGICAL X-RAY BACKGROUND

Rupert A.C. Croft[1], Tiziana Di Matteo[1,5], Romeel Davé[2], Lars Hernquist[1], Neal Katz[3], Mark A. Fardal[3], and David H. Weinberg[4]

*Draft version October 19, 2000*

## ABSTRACT

We use a hydrodynamic simulation of an inflationary Cold Dark Matter model with a cosmological constant to predict properties of the extragalactic X-ray background (XRB). We focus on emission from the intergalactic medium (IGM), with particular attention to diffuse emission from warm-hot gas that lies in relatively smooth filamentary structures between galaxies and galaxy clusters. We also include X-rays from point sources associated with galaxies in the simulation, and we make maps of the angular distribution of the emission. Although much of the X-ray luminous gas has a filamentary structure, the filaments are not evident in the simulated maps because of projection effects. In the soft (0.5-2 keV) band, our calculated mean intensity of radiation from intergalactic and cluster gas is $2.3 \times 10^{-12}$ erg s$^{-1}$ cm$^{-2}$deg$^{-2}$, 35% of the total soft band emission. This intensity is compatible at the $\sim 1\sigma$ level with estimates of the unresolved soft background intensity from deep ROSAT and *Chandra* measurements. Only 4% of the hard (2-10 keV) emission is associated with intergalactic gas. Relative to AGN flux, the IGM component of the XRB peaks at a lower redshift (median $z \sim 0.45$) and spans a narrower redshift range, so its clustering makes an important contribution to the angular correlation function of the total emission. The clustering on the scales accessible to our simulation ($0.1-10$ arcmin) is significant, with an amplitude roughly consistent with an extrapolation of recent ROSAT results to small scales. A cross-correlation analysis of the XRB against nearby galaxies taken from a simulated redshift survey also yields a strong signal from the IGM. Our conclusions about the soft background intensity differ from those of some recent papers, which have argued that the expected emission from gas in galaxy, group, and cluster halos would exceed the observed background unless much of the gas is expelled by supernova feedback. We obtain reasonable compatibility with current observations in a simulation that incorporates cooling, star formation, and only modest feedback. A clear prediction of our model is that the unresolved portion of the soft XRB will remain mostly unresolved even as observations reach deeper point-source sensitivity.

*Subject headings:* Cosmology: observations, large scale structure of Universe

## 1. INTRODUCTION

It is now well established that the Cosmic X-ray Background (XRB) results almost entirely from the integrated X-ray emission of many discrete sources. Deep ROSAT surveys have shown that a large fraction of the soft ($0.5-2$ keV) XRB is produced by active galactic nuclei (AGN), i.e. quasars and Seyfert 1 galaxies (e.g., Hasinger et al. 1998; Schmidt et al. 1998). Until recently, the nature of the sources producing the energetically dominant, hard ($2-10$ keV) XRB was largely unknown. *Chandra* has now imaged the hard (2-10 keV) X-ray sky at high resolution and resolved essentially all of the XRB in this band (down to a flux of $4 \times 10^{-15}$ erg s$^{-1}$ cm$^{-2}$; Mushotzky et al. 2000; see also Brandt et al. 2000). The optical follow-up campaigns have shown that the newly discovered XRB sources include (1) optically 'faint' galaxies, which may be either quasars at high redshifts or obscured AGN, and (2) apparently 'normal' galaxies.

[1]Harvard-Smithsonian Center for Astrophysics, Cambridge, MA 02138; rcroft,tdimatte,lars@cfa.harvard.edu

[2]Princeton University Observatory, Princeton, NJ 08544; rad@astro.princeton.edu

[3]Department of Physics and Astronomy, University of Massachusetts, Amherst, MA, 01003; nsk@kaka.astro.umass.edu,fardal@weka.astro.umass.edu

[4]Department of Astronomy, The Ohio State University, Columbus, OH 43210; dhw@astronomy.ohio-state.edu

[5]*Chandra* Fellow

However, a non-negligible fraction of the sky brightness, particularly at soft energies, may still be contributed by diffuse emission (mainly Bremsstrahlung) from intergalactic gas. Cosmological structure formation theories have been used to estimate the radiation emitted by gas in galaxy clusters (e.g., Blanchard et al. 1992). In the last few years, attention has also focused on the large fraction of baryonic matter at low redshift predicted by these theories to be in the form of a "warm-hot" ($10^5 - 10^7$K) intergalactic medium (WHIM). Detection of the faint, soft-band X-ray emission from this currently unobserved gas would help reconcile measurements of the baryon density in the local universe (e.g., Fukugita, Hogan & Peebles 1998) with the predictions of cosmological nucleosynthesis (Burles & Tytler 1998). In this paper, we use a cosmological hydrodynamic simulation to predict the intensity and angular distribution of X-ray emission from intergalactic gas. Our approach includes this relatively low density filamentary component, as well as clusters and groups. We also include a simple prescription for emission from AGN in the simulation.

Hydrodynamic simulations are routinely used to examine the expected X-ray emission from galaxy clusters in a cosmological context (see, e.g., Frenk et al. 1999 and references therein). The lower density gas in structures between clusters in such simulations is morphologically more complicated, being distributed in the usual filaments and sheets. One can ask what observational signatures of X-

ray emission are expected from this gas. For example, are the filaments visible in projection on the sky? Experience with filamentary structure in the galaxy distribution, which only stands out clearly in 3-dimensional redshift maps (e.g., de Lapparent, Geller & Huchra 1986), suggests that they will be difficult to detect. Nevertheless, some evidence has been found for diffuse filamentary emission in ROSAT deep pointings (Scharf et al. 1999). Images of individual filaments made from simulations by Pierre, Bryan & Gastaud (2000) suggest that the *XMM-Newton* telescope should be able to detect them, at least when they are considered in isolation. An alternative approach, which we undertake here, is to make simulated sky maps using the cosmological models and measure statistical properties of the X-ray flux, which can eventually be compared to observations.

Another important question is the integrated intensity of the background. Several recent papers have claimed that the expected emission from gas in groups of galaxies or galaxy halos exceeds the observed diffuse soft X-ray background by at least an order of magnitude (Pen 1999; Wu, Fabian, & Nulsen 1999). They suggest that much of the gas in these groups and galaxies halos must be expelled or inflated by supernova feedback, decreasing its density and hence its X-ray luminosity. The amount of supernova feedback required is quite extreme, approaching 1 keV per baryon. However, none of these calculations is based on self-consistent simulations including cooling and galaxy formation. It is important to see whether our simulation, which only includes very modest supernova feedback, gives similar results or is consistent with the observed X-ray background.

The layout of the paper is as follows. In §2, we present the hydrodynamic simulation and cosmological parameters used. We examine the diffuse X-ray emission from the IGM in §3, and study the relationship between X-ray emissivity and gas density. In §4, we describe our procedure for associating X-ray luminosities with some galaxies in the simulation. Simulated sky maps are generated as described in §5, and their clustering is analyzed in §6. We summarize and discuss our results in §7. Finally, in Appendix A, we explain how and why we account for the multiphase nature of the gas when calculating its X-ray emissivity, and carry out some tests of our procedure.

## 2. THE SIMULATION

Davé et al. (2000, hereafter D00) have recently studied the distribution of gas temperatures and densities in several simulations of Cold Dark Matter models. One of these is the simulation that we use here, their "D1". We refer the reader to their paper for more details on this simulation, as well as a comparison of the effects of resolution, box size, and numerical technique on the fraction of gas in different phases.

The simulation is of a cosmological constant dominated Cold Dark Matter model, run using the code Parallel TreeSPH (Davé, Dubinski & Hernquist 1997). The parameters used are $\Omega_M = 0.4$, $\Omega_\Lambda = 0.6$, a Hubble constant $H_0 = 65$ km s$^{-1}$ Mpc$^{-1}$, an amplitude of mass fluctuations $\sigma_8 = 0.8$, an initial spectral index $n = 0.95$, and a baryon fraction $\Omega_b = 0.02h^{-2}$ (Burles & Tytler 1998). The simulation volume is a cube of side-length 50 $h^{-1}$Mpc and initially contained $144^3$ dark matter particles and as many gas particles, which results in a baryonic mass resolution of $8.5 \times 10^8 M_\odot$ per particle. The spatial resolution of the simulation is 7 comoving $h^{-1}$kpc (equivalent Plummer softening), and it was evolved from $z = 49 \rightarrow 0$. A prescription for star formation converts gas particles in convergent flows in cooling, dense regions into star particles and deposits feedback energy from supernovae into the surrounding gas (see Katz, Weinberg & Hernquist 1996 for details). Because these regions are so dense, the energy rapidly radiates away and has only a limited effect on the large-scale gas morphology. Feedback from stars in the simulation is therefore relatively unimportant, something that should be borne in mind when considering the X-ray emission from clusters and other dense regions. We discuss this point further below.

In Figure 1, we plot the temperatures and densities of the gas particles in the simulation at three different redshifts. D00 have found, in their comprehensive study, that at the present day, $30 - 40\%$ of baryons are predicted to be in a WHIM, with a relatively low median overdensity of $\sim 20$ times the cosmic mean. In our calculation of the X-ray emission, all the gas above $T \sim 10^5$ K will make a contribution, with the IGM emission being dominated by the hottest cluster gas.

We can see from Figure 1 that the fraction of hot gas increases with decreasing $z$, as more gas becomes shocked and heated by falling into high density regions (the fraction above $10^5$ K climbs from 5% at $z = 2$ to 28% at $z = 0.5$ and 41% at $z = 0$).The three phases of gas identified by, e.g., Davé et al. (1999a) are clear from the Figure: a cold diffuse IGM, a shocked plume of hot gas, and a cold, condensed, collapsed fraction. We note that in this simulation no ionizing background radiation has been included, so that the lowest density gas is all at a very low temperature. The densities in the plot have been subjected to a correction to make allowances for the co-existence of two gas phases — hot/diffuse and cold/dense — in galaxy groups and clusters. The SPH algorithm tends to blur the boundary between these phases when they are in close proximity and the mass resolution is limited, and it is necessary to separate them explicitly to properly calculate the X-ray emission. We describe this correction in detail in Appendix A, and also briefly in §3 below.

## 3. DIFFUSE X-RAY EMISSION

The IGM is a hot, thin plasma that emits X-rays via a number of physical mechanisms, including Bremsstrahlung, collisional excitation of spectral lines, and recombination. Metal line emission is most important for low density, cooler gas, while thermal Bremsstrahlung dominates the emission from the intracluster medium. We use a Raymond-Smith (1977) code to calculate the X-ray emission from the IGM. Given the temperature, metallicity, and electron density of gas, the code calculates the volume emissivity. In the maps that we make, much of the radiation will come from relatively high redshift, so that redshifting into the observed band is important.

As the metallicity of the gas is not tracked self-consistently in the simulation, we assign a metallicity that is a simple function of density. For gas at the mean density, the metallicity we assign is 0.005 of the solar value, with the metallicity being proportional to $\sqrt{\rho}$ in other regions and being limited to a maximum of 0.3 $Z_\odot$. In this way, we

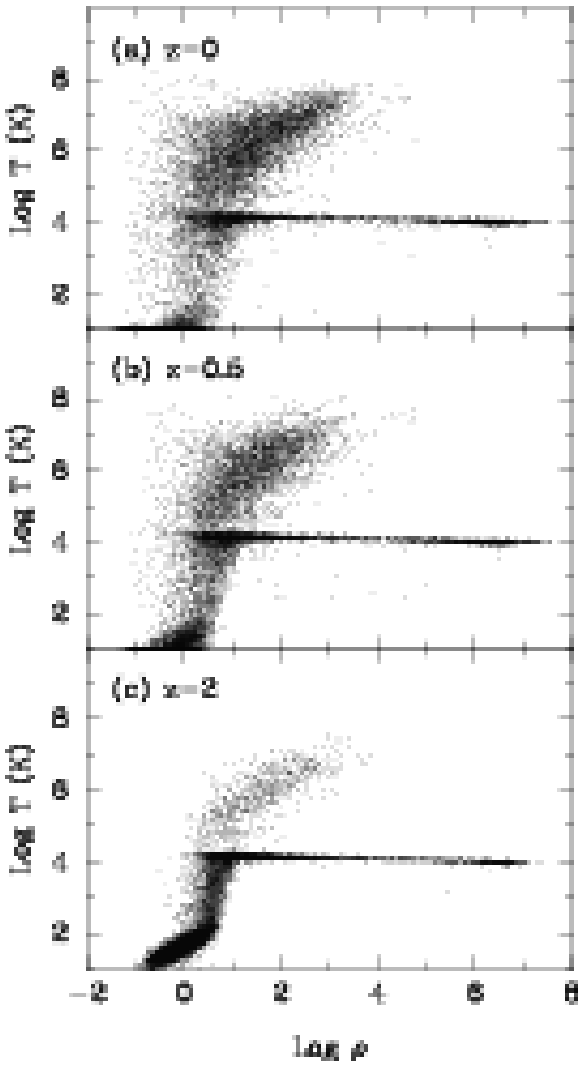


FIG. 1.— The temperature and density of gas particles in the simulation at 3 different redshifts. We plot a randomly chosen 10000 particles in each panel.

roughly mimic the simulation result of Cen & Ostriker (1999), which in turn approximately reproduces the fraction of metals found in the low density IGM at high redshift, and the metallicity of groups and clusters in the Local Universe. Another study of metal enrichment, involving several different physical models, has been carried out by Aguirre et al. (2000ab), starting from the same hydrodynamic simulation that we use here. We leave the detailed study of the effect of metal enrichment on X-ray emission (and absorption, see, e.g., Hellsten, Gnedin & Miralda-Escudé 1998 and Perna & Loeb 1998) to future work. In the present paper, we limit our study of varying metallicity to testing only the effect of removing all emission from metals.

Much of the radiation from the IGM will be in the form of relatively soft X-rays, corresponding to thermal emission from filaments, groups, and clusters, which have temperatures that range from a fraction of 1 keV to a few keV. We will make maps of emission in two separate bands, $0.5-2$ keV (soft) and $2-10$ keV (hard), spectral intervals motivated by those commonly used in the analysis of observational data. The hard band will therefore contain emission representative of only a small portion of the IGM, the hottest clusters. Below 0.5 keV, extragalactic emission becomes impossible to separate cleanly from galactic coronal emission, and galactic absorption becomes even more important. Because of this, we do not attempt to make maps or study clustering of the very soft XRB. We will, however, calculate the mean intensity in a band centered on 0.25 keV, due to the WHIM, which can be compared to X-ray shadowing measurements (e.g., Wang & Ye 1996; Cui et al. 1996).

### 3.1. *The X-ray luminosity of simulation gas particles*

The emissivity of gas is given in erg $s^{-1}$ per unit volume by the Raymond-Smith code. The simulation we have is Lagrangian, so that the gas is discretized into particles rather than cells of unit volume. To calculate the X-ray luminosity of each particle we must therefore calculate the volume of gas associated with it. First, the density for each particle is calculated using the symmetrized SPH spline kernel (see Hernquist & Katz 1989), with 32 neighbors. The volume associated with the particle is

$$V = \frac{0.76 M_g}{m_H n_H}, \tag{1}$$

where $M_g$ is the particle gas mass, $m_H$ the mass of a hydrogen atom, and $n_H$ the number density of hydrogen atoms (which are fully ionized in nearly all the hot gas we are considering). We take the fraction by mass of helium in primordial gas to be 0.24, which accounts for the factor of 0.76 for hydrogen (we use the same formula for gas of non-primordial composition, ignoring the small contribution to the mass made by metals).

A small number of the hot gas particles in clusters and groups will have many neighbors which are cold, condensed galactic gas. The intracluster gas is, however, in a separate phase, so that for the SPH density estimate to have physical meaning, we choose not to include the contribution from the cold, dense gas. Without separating out the cold galactic gas, the density of these hot particles will be overestimated. With higher mass resolution, this would not be such a problem, as the different phases would be better resolved. In the present simulation, however, this correction to the densities of the hot particles makes a large difference to the overall X-ray emission. In equation (1), therefore, we estimate $n_H$ for hot ($T > 10^5$ K) particles after removing particles that have $T < 10^{4.5}$ K and densities greater than 1000 times the mean. We use this density estimate in Figure 1 and in the rest of the results in the main text of this paper.

In Appendix A, we describe the motivation for this corrected density estimate in greater detail, and we perform a number of tests to show that it gives correct results. For previous approaches to dealing with this problem in the context of galaxy formation, the reader is referred to Pearce et al. (1999) and Ritchie & Thomas (2000).

### 3.2. *Emissivity and density*

In Figure 2, we plot the volume emissivity of particles against their density in units of the mean. We find that some X-ray emission comes from gas at low densities, at or around the cosmic mean, which is probably recently shocked gas. Most of the X-ray emitting particles have

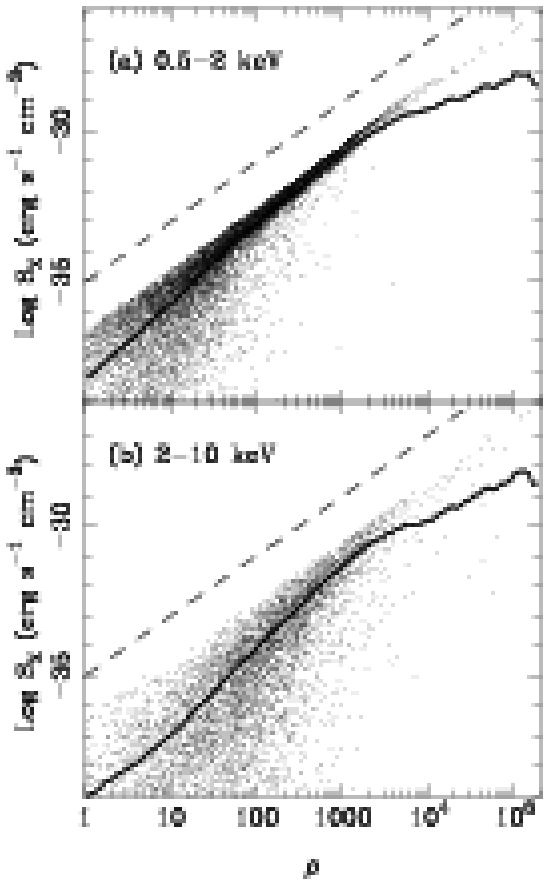


FIG. 2.— Emissivity vs. gas density (in units of the cosmic mean) at $z = 0$ in two bands (a) soft, (b) hard. The solid line is the average emissivity at a given density. The dashed line represents $S_X \propto \rho^2$, with arbitrary normalization. A randomly chosen 1% of the particles is plotted.

densities in the range $\rho = 100-1000$. The Bremsstrahlung component of the emissivity is proportional to $\rho^2 T^{0.5}$. The temperature is roughly proportional to the density in the hot diffuse gas regime (although with quite large scatter, see Figure 1 and figure 6 of D00). This results in a mean emissivity at a given density that is approximately a power-law with a slope of 2.5. At very high densities, the solid line, which represents the mean emissivity, bends downwards due to the large fraction of particles that have cooled. The scatter about the line increases at lower densities, with the slope of the upper envelope being a roughly constant $S_X \propto \rho^2$. This larger scatter at lower densities may be due to the widely differing histories of gas elements at low density, where shock heating has occurred to different extents. At higher densities, gas particles tend to relax more uniformly to the virial temperature.

We examine the spatial distribution of gas density and X-ray emission at $z = 0$ in Figure 3. To treat both in a similar way, we assign the gas mass and the X-ray emission to a two-dimensional grid using the projected SPH kernel. The X-ray emissivity per unit area in grid cell $jk$ is therefore (see also Springel, White, & Hernquist 2000)

$$\frac{1}{A}\sum_{i=1}^{N} {}^{X}S_i W_{i,j,k} \qquad (2)$$

where $N$ is the number of particles, and ${}^{X}S_i$ is the X-ray flux emitted by particle $i$ (see also Springel, White, & Hernquist 2000). $W_{i,j,k}$ is the integral of the projection of the SPH smoothing kernel in the $x-y$ plane over grid cell $j,k$. $A$ is the area of a grid cell. For the mass density assignment, we replace ${}^{X}S_i$ with the gas mass of particle

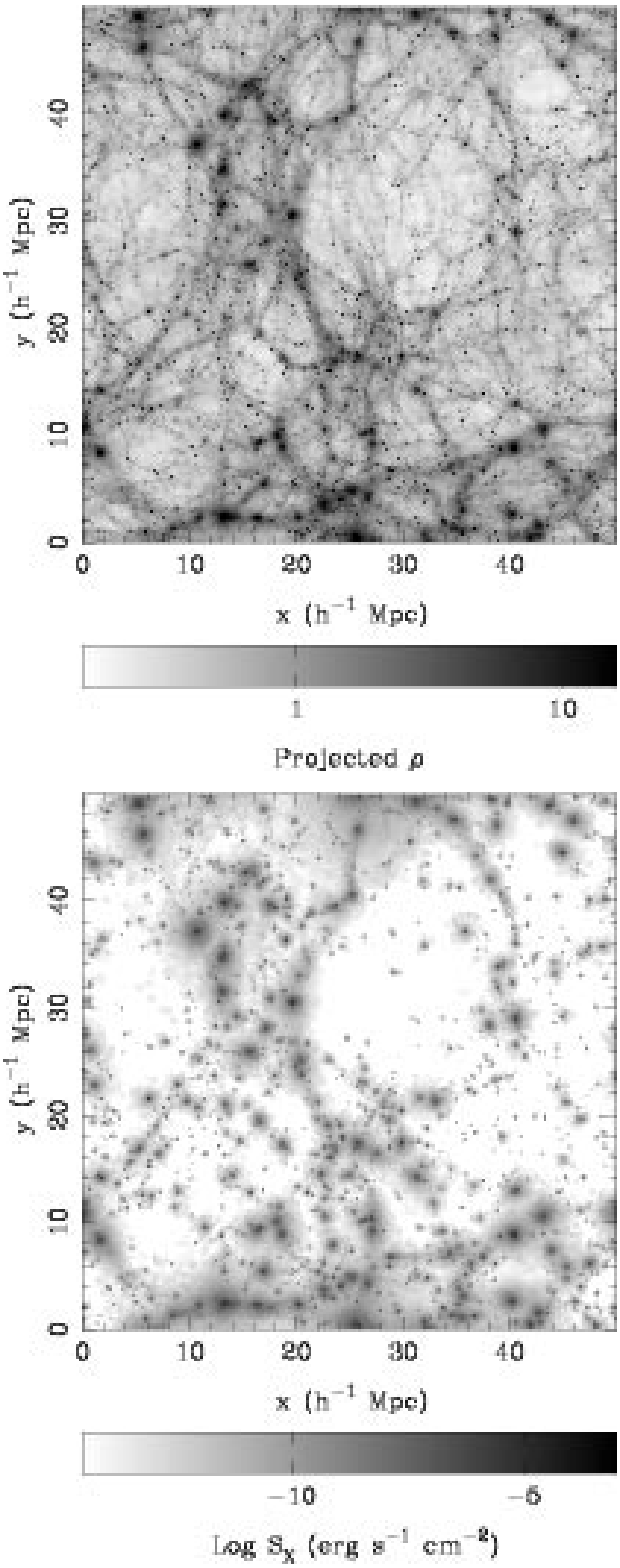


FIG. 3.— Projection of density (top) and X-ray emission in the soft band (bottom) at $z = 0$.

$i$. By using the SPH kernel in this way, we make use of the fact that we have higher spatial resolution in higher density regions. We use the same procedure in the sky maps that we present in §5.

In the case of Figure 3, because we have projected the entire simulation volume, the absolute units on the greyscale are not very useful. In relative terms, though, one can see that the dynamic range of the X-ray scale is much larger than for the mass, as one might expect, given that $S_X \propto\sim \rho^{2.5}$. X-ray filaments are therefore likely to require very faint imaging to be picked out (see Pierre et al. 2000 for simulated *XMM-Newton* imaging of individual filaments). Comparing the two maps, it is also evident that much of the fine structure and many of the small filaments seen in the mass distribution do not show up in the X-rays. The X-ray filaments seem to be even more "beaded" than the matter structures, being made up of small galaxy groups lying close together. There are also many smaller clumps of gas emitting X-rays that lie in relative isolation, in regions of lower density. We can see in the density plot that many of these are associated with individual galaxies and the emission is from gas in their halos. The X-ray luminosity function of the galaxy groups will be studied in a future paper.

## 4. ACTIVE GALACTIC NUCLEI

As mentioned in §1, AGN are the major contributors to the XRB. The hydrodynamic simulation we are using was run primarily to study galaxy formation (Davé et al. 1999b; Weinberg et al. 1999), and it therefore includes galaxies that we can use to model the AGN contribution.

The recent dynamical evidence for supermassive black holes in many nearby galaxies, and the correlations between the mass of the central black hole and the mass (Magorrian et al. 1998) or velocity dispersion (Ferrarese & Merritt 2000; Gebhardt et al. 2000) of its host bulge, provide strong support for the idea that most galaxies should contain central supermassive black holes. We therefore associate a central X-ray point source with each galaxy in the simulation and include the radiation emitted by these AGN in our X-ray maps.

Since AGN are believed to be powered by accretion onto black holes, a process far below the resolution of the simulation, we will necessarily have to treat the X-ray emission from black holes in the simulated galaxies in a simplified fashion. In the future, it may become possible to track some aspects of the merging and growth of supermassive black holes self-consistently in hydrodynamic simulations (see, e.g., Merritt, Cruz, & Milosavljevic 2000 for preliminary work along these lines).

For now, the primary role for our simulated AGN population is to be placed in our skymaps along with the more accurately computed diffuse emission, so that we can approximately gauge their effect on the overall clustering and flux level of the XRB. Even so, there is some information that can be gained about the likely nature and distribution of AGN in a CDM universe from our use of a hydrodynamic simulation.

Our study represents the first attempt to incorporate a simple scheme for AGN and their X-ray emission into the framework of hydrodynamic simulations. In recent work, Kauffmann & Haehnelt (2000, hereafter KH), Cattaneo (1999), and Wilman, Fabian & Nulsen (2000, hereafter WFN) have used semi-analytic galaxy formation models and associated prescriptions for quasar fueling to study the growth of supermassive black holes. Models by KH and Cattaneo assume that black holes are fed by cold gas during major galaxy mergers. This allows them to reproduce the B-band luminosity function of quasars, but they do not use the XRB as a constraint. WFN instead assume that quasars are fueled by Bondi accretion from the dense, hot gas phase in galaxies, and they attempt to reproduce the hard XRB and X-ray source counts.

Our approach is complementary to (albeit less ambitious than) the work in these papers. We will assume that a fraction of the cold gas in each galaxy is accreted by the central black hole and calculate its X-ray emission using current constraints on AGN X-ray spectra.

### 4.1. *Galaxy selection*

We use the SKID groupfinder (see, e.g., Governato et al. 1997) to find distinct clumps of gas and star particles. The minimum number of particles in a clump (including both cold gas and stars) before it is considered a galaxy is set to be 4, with a corresponding mass of $3.4 \times 10^9 \mathrm{M}_\odot$. At $z = 0$, there are 5500 of these galaxies in the simulation volume, although at $z = 2$, around the peak of the AGN distribution, there are only 210. We use a small mass limit to have as large a number of galaxies as possible. Below $\sim 60$ particles, the list of objects above a given mass will be incomplete. As we will in any case be sparsely sampling the galaxy distribution to find AGN and assigning their properties with parameterized prescriptions, this incompleteness is relatively unimportant for our purpose. Although the limit of 4 particles might seem low, the overdensity threshold for star formation is $\rho > 1000$, and cold gas must also satisfy this threshold to be counted in a galaxy, so the existence of a 4-particle SKID group implies the existence of a larger dense system surrounding it.

For each galaxy the simulation provides us with $M_{gas}$, the amount of cold gas in the galaxy, and $M_{star}$, the mass in stars. The ratio $M_{gas}/M_{star}$ is generally higher at higher redshift. We also have the spatial positions of the galaxies, and their halo circular velocities, $V_c$.

### 4.2. *Emission from AGN*

We use this galaxy information together with an approximate physical model to simulate the point-source X-ray emission. As mentioned above, we are forced to include somewhat *ad hoc* relationships between variables and free parameters.

By analogy with the prescriptions adopted in semi-analytical models, e.g. KH or Cattaneo, Haehnelt, & Rees (1999, hereafter CHR), we assume that the ratio of the accreted mass to total cold gas scales with circular velocity:

$$M_{acc} = f M_{gas} \left( \frac{V_c}{v_{\max}} \right)^4 , \qquad (3)$$

where $V_c$ is the halo circular velocity, and $v_{\max} = 200$ km s$^{-1}$, $f = 10^{-4}$ are free parameters chosen so that the simulated population approximately reproduces the observed AGN X-ray luminosity function at $z \sim 0$ (e.g., Boyle et al. 1998).

Another constraint on these parameters, as well as on the power-law exponent of $V_c$, is the source count measurement by the *Chandra* satellite. The $\log N - \log S$ results of

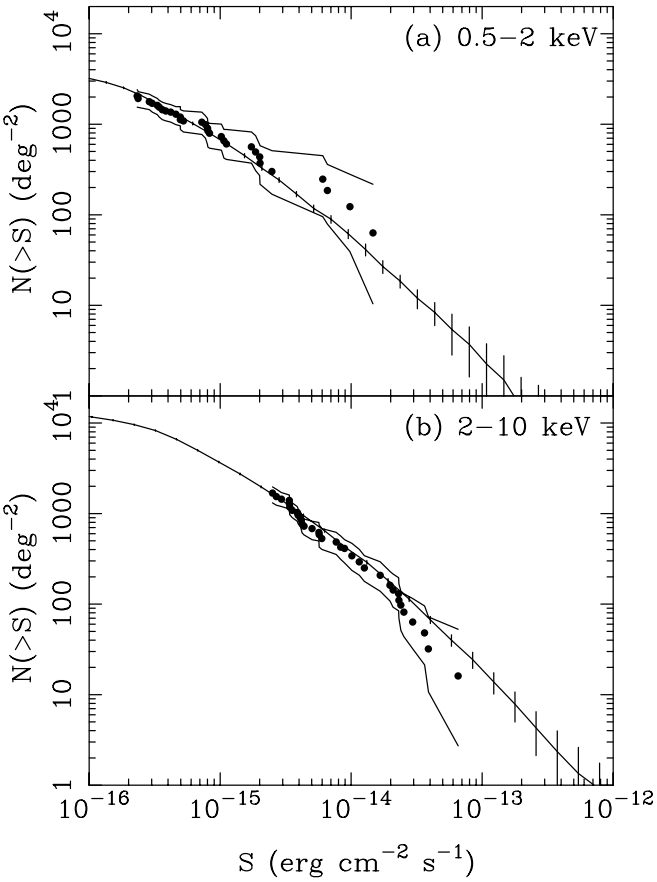


FIG. 4.— Number counts ($\log N - \log S$) for the simulated AGN (smooth solid line). The variance in results from separate survey areas of 1 degree is shown by the error bars. The *Chandra* results of Mushotzky et al. (2000) are shown as points, with their $1\sigma$ statistical errors denoted by jagged lines.

Mushotzky et al. (2000) are shown in Figure 4. The fourth power dependence on $V_c$ is stronger than that adopted by KH, but we find that such a dependence is necessary to reproduce the observational results. We will return to this point below. The strong dependence on velocity in Equation 3 may be supported by the recent work of Ferrarese & Merritt (2000) and Gebhardt et al. (2000), who find $M_{BH} \propto \sigma_v^{\sim 4}$ ($\sigma_v$ is bulge velocity dispersion) in nearby galaxies. In the framework of our model, this would imply that the mass of the black hole is built up mostly by accretion ($M_{BH} \propto M_{acc}$).

The major active phase takes a short fraction of a galaxy's lifetime. This mass is accreted on a timescale $t_{acc}(z) \sim 1 \times 10^7 (1+z)^{-2}$ yr, which we can also refer to as the quasar lifetime. The $z$ dependence in the timescale is necessary to reproduce the peak of the quasar phase and the fast fall off at $z < 2$ (see also KH and CHR). With this assumption, $\dot{M} = M_{acc}/t_{acc}$, we take the probability of a given AGN being active at redshift $z$ to be $P_{on} t_{acc}(z) |dt_H(z)/dz|^{-1}$, where $t_H(z)$ is the Hubble time at redshift $z$. $P_{on}$ is another free parameter, necessary because we must randomly sample the galaxy population, as we use the same simulation at different redshifts rather than following the evolution of individual galaxies. We do not specifically treat the effects of obscuration in AGN. The presence of a population of obscured AGN (at $z > 2$) can be relevant for producing significant quantities of hard X-rays. The properties of such sources, however, are required to be quite different from those of the established local classes of AGN, and their modeling would imply the introduction of further assumptions for the prescription of the absorbing material (see, e.g., WFN).

We take the luminosity of the nuclear source to be $L_{bol} = \eta \dot{M} c^2$. The 2-10 keV X-ray luminosity in AGN is typically equal to 3% $L_{bol}$ (Elvis et al. 1994). We assume a standard accretion disk efficiency of $\eta = 10\%$ as long as the accretion rate exceeds $\sim 1.3 \alpha^2 \dot{M}_{Edd}$ (where $\dot{M}_{Edd} \equiv L_{Edd}/(0.1c^2)$ and we assume $\alpha = 0.1$ for the disk viscosity parameter). When the accretion rate is lower than this, we set $\eta = 10^{-3}$ to allow for an advection-dominated, low luminosity phase (which turns out to be important only at $z < 1$). We set the black hole masses using the Magorrian et al. (1998) relationship (valid at these low redshifts) between bulge mass and black hole mass, assuming a bulge mass proportional to the total galaxy mass in the simulation.

The X-ray spectrum of a typical AGN ($\eta = 0.1$) is a power-law with photon index $\Gamma = 1.8$, and with an exponential cut off at 200 keV (irrelevant for 0.5 – 10 keV energies). The X-ray spectrum of the fainter sources ($\eta = 10^{-3}$) is harder, with a photon index $\Gamma = 1.4$, as expected from Bremsstrahlung emission from hot, radiatively inefficient accretion flows (and similar to that of the hard X-ray background).

Given the above model, we calculate $\log N - \log S$ for the point-source population (Figure 4). The free parameters in the model are those in equation (3), which govern the luminosity of each AGN ($f$, $v_{max}$, and the $V_c$ exponent), and are responsible for the shape and left-right movement of the $\log N - \log S$ curve. The other parameter, $P_{on}$, multiplies the probability of a quasar being on, and moves the $\log N - \log S$ curve up and down. It is degenerate in this respect with $t_{acc}$, the quasar lifetime, which we choose not to vary. As mentioned above, we have adjusted the free parameters so that our results approximately reproduce the $\log N - \log S$ measured by Mushotzky et al. (2000) (also shown in Figure 4), and the $z = 0$ QSO X-ray luminosity function (Boyle et al. 1998, not plotted).

One point to note is that equation (3), which governs the relationship between the black hole accretion rate and halo circular velocity, is required to be steep to reproduce the relatively shallow slope of the observed $\log N - \log S$ relationship. With a shallower $V_c - M_{acc}$ relation, the black hole luminosities are spread over a narrower range, and the simulated $\log N - \log S$ is much steeper. Remember that this assumed that there was no population of quasars associated with galaxies that were too small for us to resolve in the simulation (with halos $v_c \ll 100$ km s$^{-1}$). With a much higher resolution simulation, the situation could be different. However, for the bright end slope to be reproduced, we would still require a steep $V_c - M_{acc}$ relation.

## 5. THE SIMULATED SKY

Looking at relatively thin slices of a CDM universe (e.g., Figure 3) can tell us about the morphology of the simulated X-ray emission. However, to compare with observations, which give us angular positions of X-ray photons on the plane of the sky, it is necessary to make simulated sky

maps. In this way, we can see how much of the filamentary structure of the IGM is preserved when projection is taken into account, and whether any substructure in clusters arises from background material. We can quantify the predictions of our model with measurements of the angular clustering on small scales. By making maps, we can also see how the AGN point sources lie within the diffuse emission, and assess the effect of their different redshift distributions.

### 5.1. *Map making*

Our simulation volume has a side length of 50 $h^{-1}$Mpc, but X-ray emission from AGN originates from a redshift of $z = 2 - 3$, at a comoving distance 50 times as far away or more. To make maps, therefore, we must replicate our simulation volume (including a random change of viewing angle) many times. The same technique has been used before for making maps of the Sunyaev-Zel'dovich decrement by da Silva et al. (2000), Seljak, Burwell, & Pen (2000), and Springel et al. (2000), and a similar idea has been used for maps of gravitational lensing distortions by White & Hu (2000). Unlike Sunyaev-Zel'dovich maps, the X-ray maps are subject to the inverse-square law, so that emission from low redshifts will dominate the signal (particularly the clustering). This should mean that they will be less sensitive to the restrictions imposed by a small box, as at low $z$ the simulation volume only subtends a small angle. We should, however, be careful about interpreting our results, and we will be restricted to studying clustering of the XRB on small scales (separations $\theta < 20$ arcmins). We leave study of large-scale structure in the XRB to future work, when larger simulations become available. Some tests of convergence, using different box sizes and mass resolutions, have been carried out for the Sunyaev-Zel'dovich maps by Springel et al. (2000). Tests of numerical projection against analytic clustering (although not of X-ray emission) in different contexts have been presented by, e.g., White & Hu (2000) and Croft & Metzler (2000).

We have chosen a field of view 1 deg on a side to make our maps, and use $512^2$ pixels. The pixel size is therefore 7 arcsec, roughly the same width as the FWHM of the *XMM-Newton* PSF, and significantly coarser than that of the *Chandra* telescope. We do not attempt to include foreground emission or absorption in the maps, or to tailor them to any specific instrument by including instrument noise or response functions. Also, our maps do not include Poisson sampling noise from individual photon statistics, and will include structure faint enough that it will be challenging to detect with current X-ray telescopes.

We make use of 27 simulation outputs, ranging in output redshift from $z = 0$ to $z = 6$, and spaced roughly logarithmically in redshift. We have checked that there is no significant X-ray emission from beyond $z = 6$ (see e.g., Figure 11). The comoving distance to $z = 6$ is 5250 $h^{-1}$Mpc, so that we replicate the box 105 times. We work in comoving coordinates, to take advantage of the fact that light rays travel in straight lines in a flat universe. The boxes are stacked along the line of sight, using the output time closest to the redshift reached at a given point. Each box is randomized, which involves a random recentering of coordinates, and a one in two chance of a reflection about each axis. We orient the box so that one of the axes (chosen at random) lies along the line of sight, and also perform a random rotation about that axis for simulation volumes close enough to the observer that the field of view fits entirely within the box length divided by $\sqrt{2}$. Above $z = 1.4$, the simulation volume no longer subtends an angle greater than 1 deg, so that we also periodically replicate the box across the line of sight. At $z = 6$, the simulation volume has an angular extent of 0.55 deg.

To assign the X-ray flux from the particles to the sky we again use the projected SPH smoothing kernel (equation 2), to preserve the high spatial resolution of the simulation

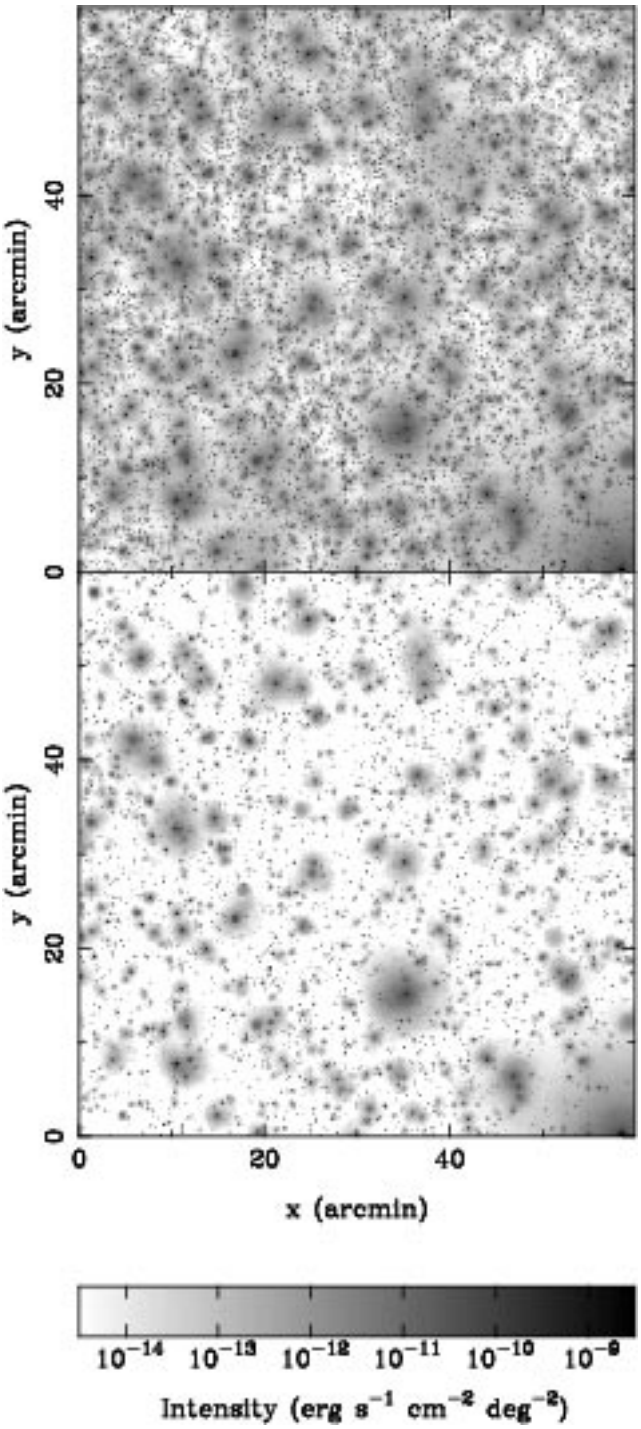


FIG. 5.— Maps of diffuse emission in the soft band (top) and hard band (bottom).

in dense regions. For the AGN point sources, we assign the fluxes to individual pixels. In the Figures showing maps which include AGN, we have convolved the AGN with a finite PSF (Gaussian with 7 arcsec FWHM) to make them stand out. In our statistical analysis of the maps, however, we do not do this. We calculate the luminosity distance for sources using the analytic approximation given by Pen (1999b).

We make several different sets of maps, in both the soft band (0.5-2 keV) and the hard (2-10 keV). To gauge the contribution of different components, we make maps with either IGM gas that includes metals (using the metallicity-density relationship of §3), or without metals, and other maps including only IGM gas with temperatures between $10^5$K and $10^7$K (the WHIM). As before, we make no distinction between the intracluster and intragroup medium and the IGM. We also make maps of the AGN component, and maps that are a sum of the AGN and IGM maps, which will represent the overall prediction for the XRB. Each set contains 20 maps, which are generated by using different random seeds for the box randomization procedure.

As mentioned before, one aspect that we do not include explicitly in our maps is the absorption of X-rays by neutral hydrogen, either in our galaxy, or elsewhere. We have chosen the lower end of our soft band (0.5 keV) so that the predictions can be compared to observed measurements without large corrections for absorption. Absorption in distant systems along the line of sight will have too small a filling factor to have an effect on our maps. As far as internal absorption in the AGN sources or their host galaxies is concerned, we have normalized our simple model (§4) using the observed $\log N - \log S$ distribution, so that any such absorption will be included implicitly, degenerate with the other parameters that govern the model.

### 5.2. *Maps*

Example IGM maps (including the contribution of metals), for the soft and hard bands are shown in Figure 5. We can see that there is much more diffuse emission in the soft band, as we might expect, with only clusters showing up in the hard band. Filaments are not as clearly seen in the soft band maps as in the single box plot (Figure 3) owing to dilution by projection. There are some vaguely elongated structures that might be filaments, particularly on the right side of the map. We examine them in more detail below. We can also see evidence of substructure in the dense cluster regions.

To understand which features in Figure 5 are coming from which redshift, we create a map of flux-weighted redshift. To make it, we assign the redshift of each particle multiplied by its X-ray flux to the sky grid. We then divide out this map by the X-ray flux map. We have done this for the soft X-ray band (IGM only), and we show it as Figure 6, which can be directly compared to the top panel of Figure 5. By doing this comparison, we can see that what appears to be a filamentary structure on the right-hand side of Figure 5 is composed of emission from several different redshifts ranging from $z \sim 0.3 - 1.0$, and its appearance is a chance result of projection. It is also evident that what appears to be "substructure" in the galaxy clusters (for example the nearby object in the bottom right hand corner) is also due to projection. The spatial pattern

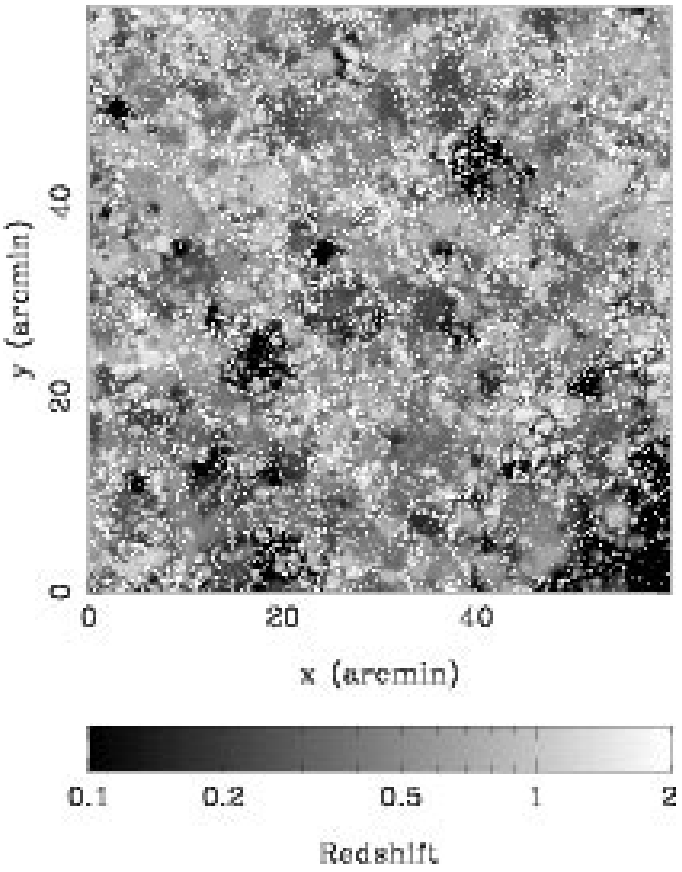


FIG. 6.— Flux-weighted redshift (for diffuse emission in the soft band only).

of $z$ in Figure 6 is interesting in itself. The map is dominated by many coherent, fairly round patches of extent $\sim 5$ arcmin, which are clusters and groups at $z \sim 0.2$ to $z \sim 1$. These are ringed by more granular emission from the IGM at higher redshifts. We will study the contribution to the total XRB arising from different redshifts and different components in §5.3 below.

In Figure 7, we show maps of the AGN part of the XRB. There is not anywhere near the amount of structure evident in the IGM maps. We will see later that the flux from AGN peaks at a higher redshift, hence angular scales correspond to larger physical scales, scales where there is not so much clustering. Our simulations cannot be used to study clustering in the AGN component on larger scales, owing to the small box size. Also, field to field fluctuations will be underestimated by missing power on scales greater than 50 $h^{-1}$Mpc.

The $\log N - \log S$ plot (Figure 4) was made using the sources that contribute to maps like Figure 7. As we expect from the source counts, there are many more sources visible in the hard band. There are approximately 5000 sources for each 1 deg$^2$ in the soft band with fluxes $> 10^{-17}$ erg s$^{-1}$ cm$^{-2}$, and 16,000 sources in the hard band. Below this flux limit, the source counts stay fairly flat, because there are no small galaxies in the simulation to host "mini-AGN." If such a population exists, the host galaxies would be below our resolution limit. As we will see later,

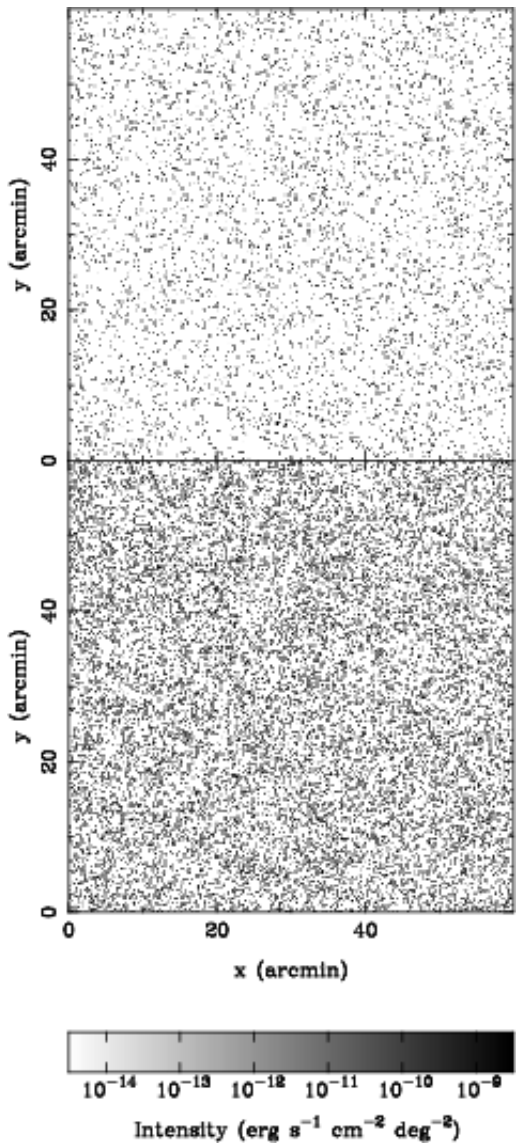


FIG. 7.— Maps of point source emission in the soft band (top) and hard band (bottom). To make the sources stand out, we have applied a Gaussian PSF with a FWHM of 7 arcsec in this plot (not used in Figure 5).

a new population of miniquasars that contribute substantially to the XRB is unlikely in the context of our model, as inclusion of X-rays from the diffuse IGM component already brings the total flux up to, or even slightly over, the observed level. However, it is important to bear in mind that this assumes that the IGM model is the correct one. The contribution from the IGM could be made smaller if we included stronger feedback, for example, which would leave room for more faint AGN. Whether this is the case or not can be addressed both by deeper imaging of the XRB, to look for point sources, and by comparing model predictions with other properties of the XRB, such as its clustering and spectrum.

The summed flux from the AGN which make up Figure 7 is much greater than that from the IGM component,

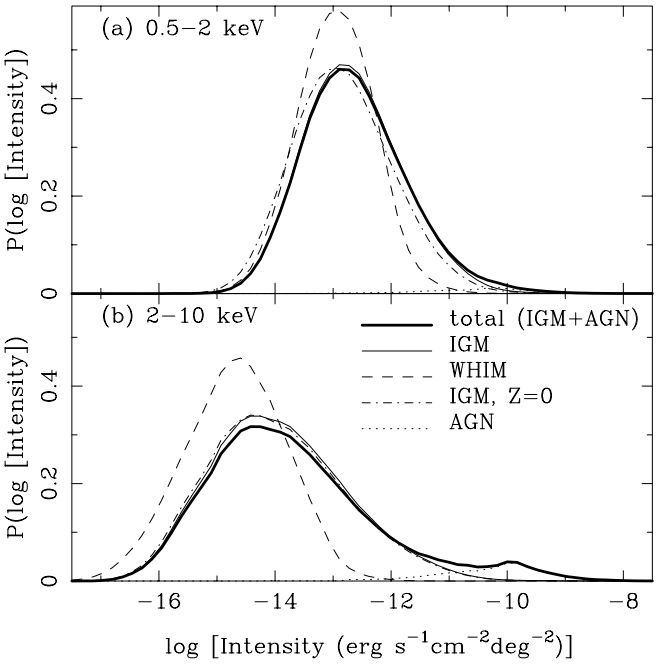


FIG. 9.— Probability distribution function of map pixel values for the soft (top) and hard (bottom) bands.

(see §5.3 below), although the great majority of sky pixels contain no AGN flux, even at the relatively low resolution of our maps.

The maps of the total XRB are shown in Figure 8, where we can compare the relative brightness of the AGN and IGM components. We have again used a 7 arcsec PSF for the AGN, to make them more visible. Even so, the AGN in the soft map are not very noticeable. Of course, the main reason for this is that the map contrast level is set to highlight features that are very faint. The surface brightness in the soft band at the edges of clusters and groups, where the emission trails off into the general IGM, is $< 10^{-12}$ erg s$^{-1}$ cm$^{-2}$deg$^{-2}$. For comparison, Scharf et al. (2000) have found evidence for a filament with surface brightness $\simeq 6 \times 10^{-13}$ erg s$^{-1}$ cm$^{-2}$deg$^{-2}$ in a deep ROSAT PSPC field.

The typical surface brightness levels of the map pixels can be seen from Figure 9, where we plot the probability distribution of pixel values (using 7 arcsec pixels for all components). We show as separate curves the total XRB, and the PDFs computed using IGM and AGN emission separately. We also show histograms for the WHIM on its own, and the IGM without the contribution of metals. The median surface brightness of the total XRB in the soft band is $1.7 \times 10^{-13}$ erg s$^{-1}$ cm$^{-2}$deg$^{-2}$, compared to $1.0 \times 10^{-14}$ erg s$^{-1}$ cm$^{-2}$deg$^{-2}$ for the hard band, but the distribution of pixel values is much wider for the latter. We will see later that this manifests itself in a higher clustering level for the hard IGM emission, although this is canceled out in the clustering of the total emission by the much brighter and more uniform AGN component. The WHIM curve is noticeably offset for the hard band, indicating as we would expect that this gas makes little contribution. We will examine the average intensity and compare to some observational determinations in §5.3 be-

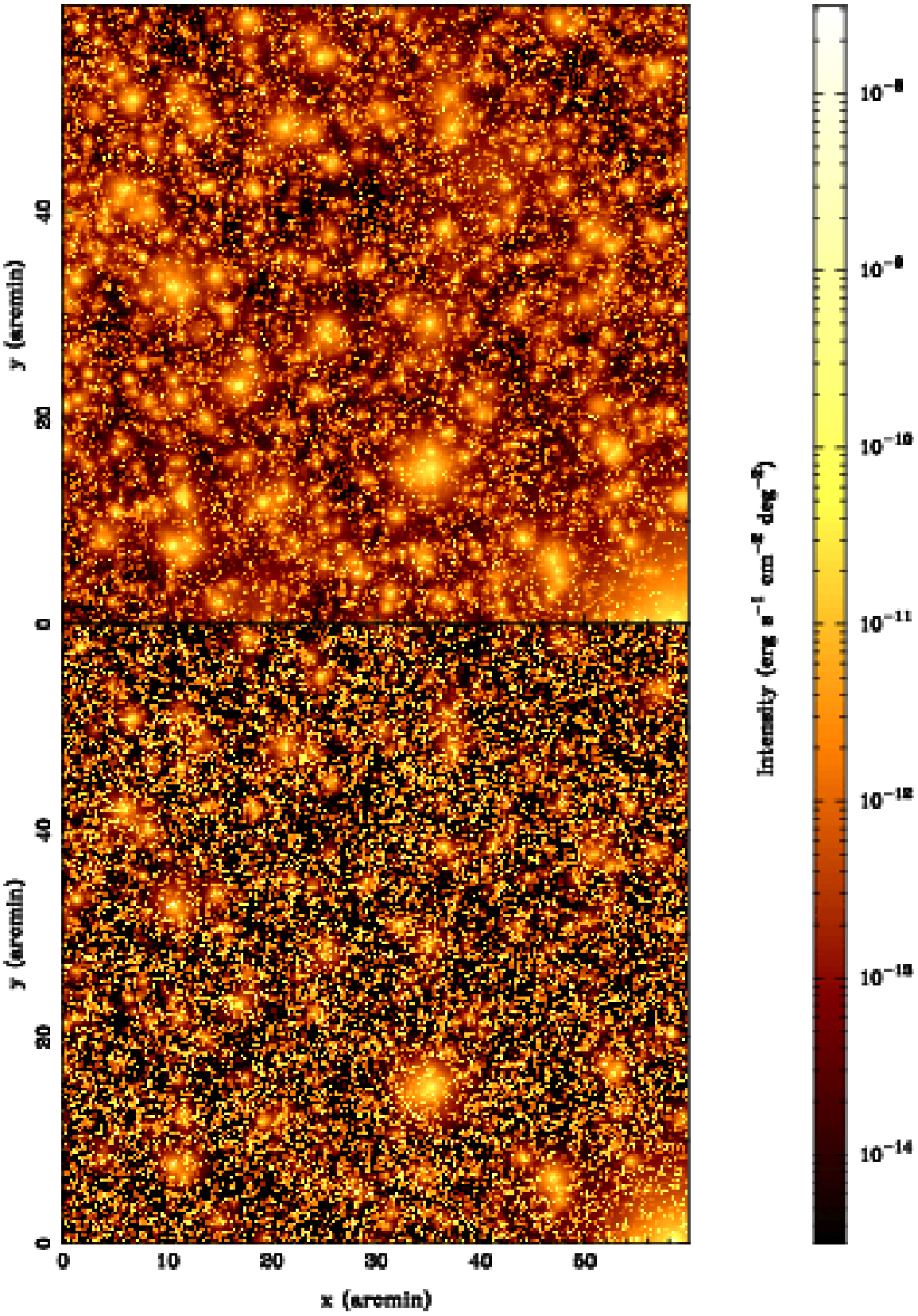


FIG. 8.— Maps of total (diffuse + point source) emission in the soft band (top) and hard band (bottom).

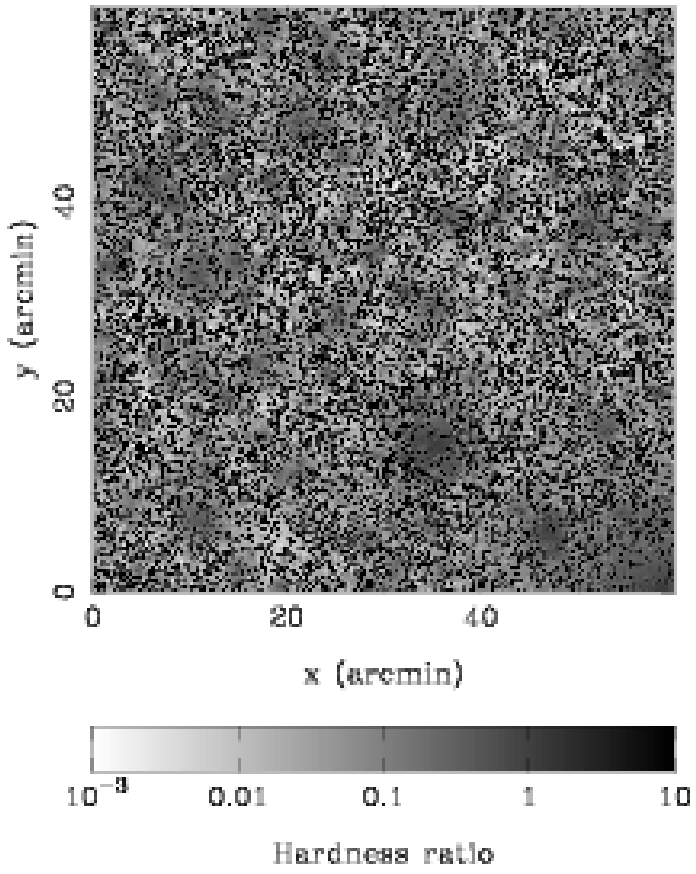


FIG. 10.— Hardness ratio (hard band/soft band flux), for the total XRB map (AGN+IGM, Figure 8).

low.

We also plot spectral information by mapping the hardness ratio (HR). We define this quantity to be the hard band flux divided by the soft band flux, and show the results in Figure 10. From the plot, it is obvious that the AGN have much harder spectra than the IGM (even harder than gas in the center of clusters). Because of the way the relative sizes of the soft and hard bandpasses are defined, none of the IGM emission has a HR $\gtrsim 0.5$. A small dynamic range in HR covers the difference between cluster centers and the more diffuse material in the outskirts. This latter material, therefore, shows up more dramatically in the HR map than in the maps of Figure 5. As we expect, the majority of the sky area is soft, with a HR of 0.01 and below, even though the total flux is higher in the hard band (due to the AGN). Because we are dividing one map by another, very deep integrations would be needed to recover any detail in the faint, soft regions. Averaging over fairly large areas of the map should enable us to recover some information about the temperature and density distribution of the diffuse IGM.

One subtle effect that might be worth exploring is the way clumps of IGM at different redshifts have different hardness ratios because of the shifting bandpass. The spectral information present may give hints as to the redshift distribution of the diffuse emission, although, of course, this will be convolved with differences in HR due to temperature variations.

### 5.3. *Mean total intensity*

In Table 1, we give the averaged total intensity in the XRB from our 20 maps. We also give results for the different components (AGN, WHIM, IGM, IGM with zero metallicity) taken separately, as well as the dispersion in results taken from the scatter in the 20, one degree fields.

The AGN are dominant in both bands, accounting for 65% of the soft-band emission and 96% in the hard-band. Of the IGM fraction of the XRB, line emission from metals accounts for 24% of the flux. In the hard band, as expected, the Bremsstrahlung contribution is higher, so that only 7% is produced by the metals. The WHIM (intergalactic gas with temperatures between $10^5$ K and $10^7$ K) is responsible for 18% of the soft-band flux coming from the IGM.

If we compare to observations, we are most interested in the situation in the soft-band. Our total soft band XRB flux is close to the *Chandra* results of Mushotzky et al. (2000), who find $6.0 \pm 1.5$ erg s$^{-1}$ cm$^{-2}$deg$^{-2}$ for $0.5-2$ keV, compared to our 6.58 erg s$^{-1}$ cm$^{-2}$deg$^{-2}$.

For the percentage contributed by AGN, we compare to the ROSAT Lockman hole observations of Hasinger et al. (1998) and Schmidt et al. (1998), as well as the sources in Mushotzky et al. (2000) for objects at fainter flux limits. The ROSAT work resolved $68-81\%$ of the soft XRB above a point source flux limit of $10^{-15}$ erg s$^{-1}$ cm$^{-2}$ into AGN. Mushotzky et al. (2000) find that $6-13\%$ more of the XRB is resolved when they push to a flux limit that is $\sim 5$ times fainter. Combining these results, from $74-94\%$ of the soft XRB flux is observed to be in discrete sources. These figures are, however, not for the $0.5-2$ keV band but for a band from $1-2$ keV, which we would expect to be slightly more dominated by AGN. Accounting for this slightly different band raises the AGN fraction in our simulation, and we predict an AGN fraction 72%, which is $\sim 1\sigma$ less than the observational estimate. We conclude that our simulation slightly overpredicts the diffuse component of the XRB, but given the observational and numerical uncertainties the level of agreement is quite encouraging.

In the hard band, a large angle survey by Marshall et al. (1980) using HEAO1 A2 data found an average intensity of $1.6-2.3\times10^{-11}$ erg s$^{-1}$ cm$^{-2}$deg$^{-2}$, compared to our total intensity of $2.6\times10^{-11}$ erg s$^{-1}$ cm$^{-2}$deg$^{-2}$. Mushotzky

TABLE 1
MEAN XRB INTENSITY. The error quoted is the dispersion in 1 deg fields, and not the error on the mean.

| Component | 0.5-2 keV band erg s$^{-1}$ cm$^{-2}$deg$^{-2}$ | 2-10 keV band erg s$^{-1}$ cm$^{-2}$deg$^{-2}$ |
|---|---|---|
| Total | $(6.58 \pm 0.88) \times 10^{-12}$ | $(2.60 \pm 0.16) \times 10^{-11}$ |
| IGM | $(2.29 \pm 0.43) \times 10^{-12}$ | $(9.67 \pm 3.90) \times 10^{-13}$ |
| IGM Z=0 | $(1.74 \pm 0.34) \times 10^{-12}$ | $(8.99 \pm 3.80) \times 10^{-13}$ |
| WHIM | $(4.15 \pm 0.55) \times 10^{-13}$ | $(1.47 \pm 0.41) \times 10^{-14}$ |
| AGN | $(4.29 \pm 0.76) \times 10^{-12}$ | $(2.50 \pm 0.16) \times 10^{-11}$ |

et al. (2000), with the high resolution of the *Chandra* satellite, were able to resolve $56-81\%$ of the hard-band XRB sources, above a flux limit of $2.5\times10^{-15}$ erg s$^{-1}$ cm$^{-2}$. Given that we chose the parameters for our simulated AGN to reproduce the Mushotzky et al. $\log N-\log S$ relation, we expect the total flux from our AGN to be consistent with the AGN data in the hard band. Because we have sources in our simulation that are fainter than the Mushotzky et al. limit, even more (96%) of our 2-10 keV XRB comes from AGN, with only a small hot cluster contribution making up the remainder.

If we consider radiation at lower energies than our soft band, galactic absorption and coronal emission become extremely important. We therefore do not plot any maps of emission in a softer band, as its clustering is likely to be too difficult to measure observationally. We have, however, computed the mean intensity due to the IGM in the band centered on 0.25 keV ($0.1-0.4$ keV), and find a value of $1.9\times10^{-12}$ erg s$^{-1}$ cm$^{-2}$deg$^{-2}$, which is 13 keV s$^{-1}$ cm$^{-2}$ sr$^{-1}$keV$^{-1}$ in the units used by the observational papers.

These papers report on the use of shadowing by foreground neutral hydrogen to estimate the extragalactic flux in the very soft X-rays. Cui et al. (1996) found 95% lower and upper limits at 0.25 keV energies of 32 keV s$^{-1}$ cm$^{-2}$ sr$^{-1}$keV$^{-1}$ and 65 keV s$^{-1}$ cm$^{-2}$ sr$^{-1}$keV$^{-1}$. They state that at least 30 keV s$^{-1}$ cm$^{-2}$ sr$^{-1}$keV$^{-1}$ has been resolved into discrete sources, so that $\lesssim 15$ keV s$^{-1}$ cm$^{-2}$ sr$^{-1}$keV$^{-1}$ must be due to the IGM. Warwick & Roberts (1998), in a review, give estimates of $20-35$ keV s$^{-1}$ cm$^{-2}$ sr$^{-1}$keV$^{-1}$ for the total intensity, from which Wu, Fabian & Nulsen (1999) deduce that $<4$ keV s$^{-1}$ cm$^{-2}$ sr$^{-1}$keV$^{-1}$ can be due to a diffuse component. At a slightly higher energy, 0.7 keV, Wang & Ye (1996) find an intensity of 28 keV s$^{-1}$ cm$^{-2}$ sr$^{-1}$keV$^{-1}$, with $<14$ keV s$^{-1}$ cm$^{-2}$ sr$^{-1}$keV$^{-1}$ expected to be due to discrete sources. As with emission in the 0.5–2 keV band, the simulation therefore gives results for diffuse emission in a softer band that are close to, or maybe slightly higher than, the observations.

### 5.4. *Intensity versus redshift*

In Figure 11, we show the intensity in the XRB emitted below a given redshift, for the different components. The values quoted in Table 1 correspond to the intensity reached by $z=6$, on the right side of the plot.

In the soft band, the IGM emission dominates for $z\lesssim 1.5$, above which it makes no significant contribution. The median redshift of total emission in this band is $z=1.1$, and for the IGM component it is $z=0.45$. If we consider the differential amount of emission per unit redshift (not plotted), the IGM XRB intensity peaks at $z\sim0.2$ and then declines fairly slowly, reaching $\sim\frac{1}{3}$ of its peak value at $z=1$. Because the IGM dominates at low $z$, there will be significant clustering due to it in the soft band, which we have already seen in the maps, and which we will quantify below. Bandpass shifting affects the fraction of WHIM emission in the IGM, which declines slightly as we move to higher redshift, as seen in Figure 11.

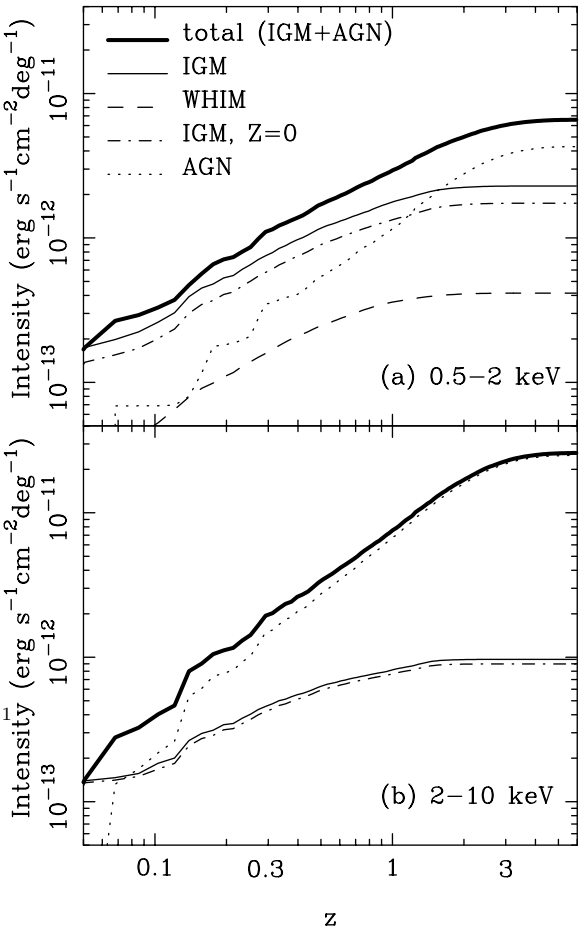


FIG. 11.— Cumulative flux as a function of redshift in the soft (top) and hard bands (bottom). We show the contribution of AGN, diffuse gas, diffuse gas without the contribution of metal line emission, and gas between $10^5$ and $10^7$K, as lines of different types.

## 6. ANGULAR CLUSTERING

### 6.1. *The autocorrelation function*

We quantify the amount of clustering on different angular scales in our maps using the angular autocorrelation function, $w(\theta)$. Our estimator is

$$w(\theta)=\langle\delta_X(\mathbf{r})\delta_X(\mathbf{r}+\theta)\rangle, \tag{4}$$

where $\mathbf{r}$ is the angular coordinate of the center of a map pixel, and $\delta_X(\mathbf{r})=[I_X(\mathbf{r})/\langle I\rangle]-1$, where $I_X(\mathbf{r})$ is the X-ray intensity in that pixel. We apply the estimator to the individual 7 arcsec pixels for small $\theta$, but regrid the maps to coarser pixels on larger scales to make the calculation faster. We have checked that both estimates match in an overlap region as expected.

The results are shown in Figure 12. In the soft band, $w(\theta)$ for the IGM alone is roughly a power law with an index of $-1.4$, and falls away on large scales. As with all such measurements, we should be careful about interpreting the large-scale points, because they will be compromised by the small box size. For example, 10 arcmin corresponds to $\sim4$ comoving $h^{-1}$Mpc at $z=0.45$, the median redshift of the IGM emission. The AGN component yields hardly any signal, so the clustering of the total XRB is basically that of the IGM diluted by a factor of $0.35^2$ (where 0.35 is the ratio of total intensities in the IGM and the total XRB). Measurements of strong clustering in the XRB on these scales, therefore, point towards the existence of baryons in the diffuse IGM, and in galaxy clusters (Blanchard et al.

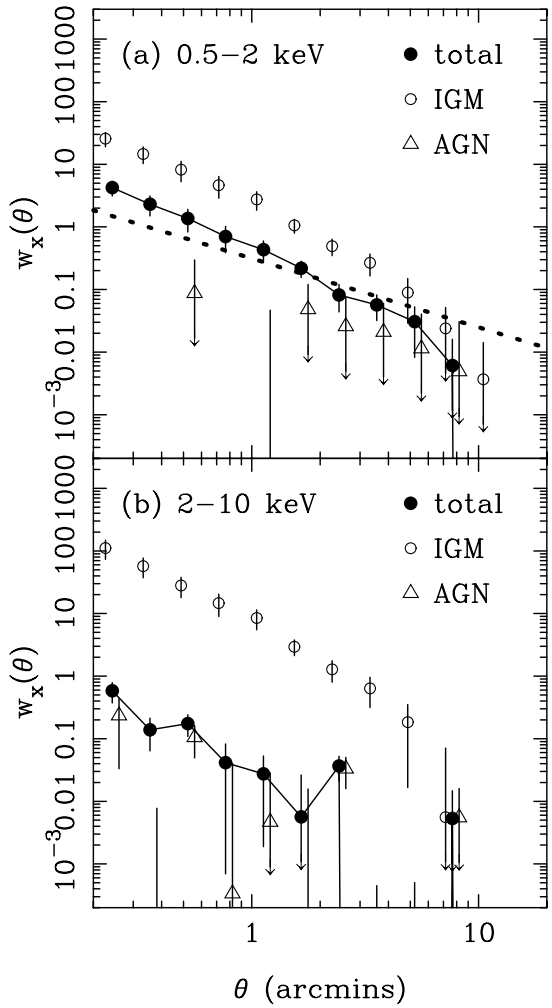


FIG. 12.— The angular correlation function of the XRB. We show results calculated from the IGM and the AGN maps separately, as well as for the summed map. The error bars are the error on the mean calculated from the scatter between measurements from 20 different maps each of area 1 deg$^2$. The dotted line is a power-law fit to the ROSAT All-Sky survey results of Soltan et al. (1999). This fit was measured from data on angular separations from 20 arcmin to 20 deg., so that the range of scales we show here represents an extrapolation.

1992; Soltan et al. 1996).

Published observational data is available on slightly larger scales than those we are able to measure here. Soltan et al. (1999) have estimated $w(\theta)$ from the soft band ROSAT All-Sky Survey for $\theta > 20$ arcmin, finding approximately a power law of slope $-1.1$. In making these measurements, Soltan et al. removed the galactic component of the XRB, which introduces major uncertainties related to the possible presence of residual fluctuations. They made no attempt to remove distinct sources, so that we can compare directly with our "total" results, by extrapolating their results to smaller scales (the dotted line in Figure 12). We find reasonable agreement, about as good as can be expected, given that it is an extrapolation, and that there are uncertainties on both sides. If only the AGN component contributed to the clustering, the simulation would lie at least a factor of five too low. On the larger scales actually probed by the Soltan et al. measurement, it seems likely that AGN come to dominate the clustering, given that the slope of the (very noisy) AGN $w(\theta)$ appears to be flatter. Larger simulations are needed to verify this, however, since the finite size of the simulation volume tends to suppress both IGM and galaxy correlations on large scales.

In the hard band, the IGM component has a higher clustering level than in the soft X-rays, because only the highly clustered central regions of relatively bright clusters are being sampled. However, because the AGN fraction of the XRB is much higher (96%), this IGM clustering is suppressed very strongly when we consider the total XRB. The AGN seem to have detectable clustering on smaller scales than in the soft band, probably because of the higher space density of hard band sources. The total $w(\theta)$ is not much higher than the AGN $w(\theta)$ value. Note that the clustering properties of the galaxies in the simulations are consistent with observations both at low and high redshift (Davé et al. 2001), so our inferred clustering of the AGN should be realistic.

### 6.2. *Cross-correlation of the XRB with nearby galaxies*

We have seen that much of the IGM emission in the simulated maps occurs at low redshift. One way to check that this is also true in the observations is to cross-correlate the XRB intensity with low redshift galaxies. Such an analysis was carried out by Soltan et al. (1997), using the ROSAT All Sky Survey and bright local galaxy catalogs. The angular cross-correlation function was measured on larger scales than we are able to simulate, and a significant signal was measured. Here we carry out an analysis of the cross-correlations on small scales, with a deeper simulated galaxy survey.

In §4, galaxies were picked from the simulation and a fraction of them denoted to have AGN. We will use the same initial set of galaxies here but restrict ourselves to a complete sample uncompromised by numerical resolution, i.e. ones that contain 60 or more particles. We use these galaxies to make a low redshift flux-limited sample by assigning a luminosity to each galaxy proportional to its stellar mass, and then applying a lower flux limit so that the mean redshift of all the remaining galaxies is 0.2. We do the same for 20 different surveys of one degree fields, generated using the same randomization parameters as the X-ray maps (§5.2). The same flux limit is used for all 20 surveys, which contain on average $\sim 500$ galaxies each.

Our estimator for the cross-correlation function, $w_{Xg}(\theta)$, is analogous to that used for the autocorrelation function (equation 4), so that we have

$$w_{Xg}(\theta) = \langle \delta_X(\mathbf{r}) \delta_g(\mathbf{r}+\theta) \rangle, \qquad (5)$$

where $\delta_g(\mathbf{r}) = [\rho_g(\mathbf{r})/\langle\rho_g\rangle] - 1$, and $\rho_g(\mathbf{r})$ is the galaxy surface density.

We show the results in Figure 13. As with $w(\theta)$, there is a stronger signal in the soft band, despite the fact that the mean galaxy redshift is significantly lower than the median redshift of the emission. Observing the cross-correlation of the XRB with galaxy samples of different mean redshift would be one way of studying the redshift distribution of the IGM emission.

## 7. SUMMARY AND DISCUSSION

We have examined the distribution of X-ray emission from intergalactic gas in a hydrodynamic simulation of a

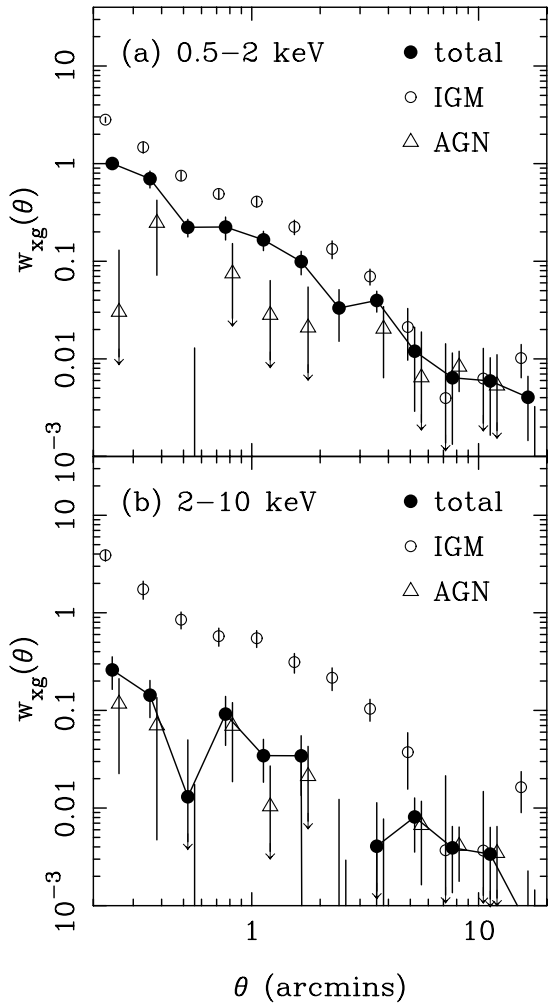


FIG. 13.— The angular cross-correlation function of galaxies and the XRB.

CDM model dominated by a cosmological constant. We also selected a certain fraction of galaxies in the simulation to have active nuclei, and calculated the X-ray emission from these AGN using a simple model with free parameters tuned to fit observed source counts. We projected the simulation volume, including dimming and redshift evolution to make artificial sky maps.

Some of our main conclusions drawn from an analysis of these maps are that:

(a) The mean total XRB intensity in the soft ($0.5-2$ keV) band, is $6.58\,\mathrm{erg\,s^{-1}\,cm^{-2}deg^{-2}}$, with 35% being generated by the diffuse IGM: clusters, filaments and groups. 50% of this IGM emission comes from below a redshift of $z = 0.45$, and the XRB coming from $z > 1.5$ is almost entirely due to AGN. The mean intensity is in reasonable agreement with the observational value ($6.0 \pm 1.5\,\mathrm{erg\,s^{-1}\,cm^{-2}deg^{-2}}$). The fraction of the total due to the IGM is slightly overpredicted by the simulations, as observationally less than $\sim 25\%$ has yet to be resolved into discrete sources.

(b) In the hard ($2-10$ keV) band, only 4% of the emission comes from the IGM, with the median redshift of XRB emission being $z = 1.5$. The total intensity is in agreement with observations, as is the IGM fraction ($\lesssim 40\%$ observationally).

(c) Because of projection, it is difficult to see any evidence for the filamentary emission, although this structure is obvious in thin slices taken through the simulation. Diffuse emission from relatively low densities does, however, cover much of the sky, and the median soft-band intensity of map pixels is $1.7 \times 10^{-13}\,\mathrm{erg\,s^{-1}\,cm^{-2}deg^{-2}}$.

(d) The clustering measured from the maps is strong on the small scales we are able to simulate ($< 20$ arcmin), and fairly close to an extrapolation of ROSAT All Sky Survey results to these scales.

(e) The angular cross-correlation of the simulated X-ray sky with simulated bright galaxy catalogs also yields a strong signal.

The procedure that we have presented here for making XRB predictions probably represents the best that can be achieved using the hydrodynamic simulation available to us at present. It will be subject to many possible improvements once more and larger simulations can be used. One aspect that should be tested if we are to achieve more precise results is the effect of box replication on the maps. We are using the same simulation, repeated along the line of sight in the maps we have made here. This should not have any adverse effect as long as clustering on the box scale is linear and as long as the contribution of matter clustering on scales larger than the box is not significant. Our present box of size $50\ h^{-1}$Mpc is certainly smaller than one would like, although the non-linearities on the scale of the box evident in Figure 3 are not necessarily severe, because only a tiny fraction of the box at these low redshifts contributes to the maps. In the future it will become possible to run convergence tests of box size on the results, and also use different phase simulations along the line of sight. Our results on the small scales we have concentrated on here should not change significantly. For example, Springel et al. (2000) give evidence that Sunyaev-Zel'dovich map fluctuations have converged in a similar box size to ours.

Another reason to use a larger simulation volume is so that we do not under represent rare objects such as rich galaxy clusters, which will account for a large fraction of the emission. Because of this, the estimate of the XRB intensity from our relatively small simulation is more likely to be an underestimate than an overestimate. The maps we have made in this paper are not useful for studying the high luminosity tail of the emission, or individual large clusters.

Higher mass resolution would help us to represent the separate hot and cold gas phases more faithfully. This would improve the situation that results when hot IGM particles are close to clumps of cold galactic gas and are therefore assigned unrealistically high densities. We have investigated this problem and its effects on the X-ray emission in detail in Appendix A. The solution we have adopted with the present simulation is to separate the cold dense particles from the hot IGM after the simulation was run, and recalculate the densities, before calculating the X-ray emission. We have tested this technique in Appendix A to show that it is robust and gives the correct result. In the future, a different approach to calculating the SPH densities could help, and if it were incorporated into the running of the simulation it may have some effect on galaxy formation by removing some artificially enhanced cooling.

Simulations with higher mass resolution would also be very useful to gauge the effect on the total X-ray flux.

With finite resolution, one will miss small objects, and smooth out the cores of larger ones, which will yield an underestimate of the mean X-ray emissivity. That this should not be severe problem is indicated by the study of D00, who show that a substantial fraction of the X-ray emitting gas remains diffuse, with little variation between simulations that use widely varying numerical techniques and have very different mass and spatial resolutions. We have also carried out a modest resolution test, described in §A.4 below. Although we have only one relatively large group at high resolution, we find that its luminosity is only 75% larger than the mean for comparable low resolution groups, even though the mass resolution is 8 times better. Lower mass groups make very little contribution to the average XRB.

The question of how much differing levels of feedback from galaxies affects the IGM X-ray emission is something we have not investigated in this paper. It has been shown in other simulations (e.g., Pierre et al. 2000; Springel et al. 2000) that non-gravitational heating can potentially drive the IGM out of small groups of galaxies and add to the more diffuse component. Some sort of strong feedback is also often invoked as being necessary for the observed cluster temperature-luminosity relationship to be reproduced (e.g., Kaiser 1991; Metzler & Evrard 1994; Bryan & Norman 1998). The simulation we use here includes star formation, and a mechanism for returning the energy of supernovae as thermal feedback to the IGM (see Katz et al. 1996 for details). Because of the high spatial resolution of the SPH code, this feedback energy is deposited in very dense regions, and it is quickly radiated away, having only a minor effect on the IGM dynamics. Despite the modest role of feedback, a large fraction of gas with soft XRB temperatures is diffuse, having not yet fallen into virialized structures, and is heated by shocks. As shown by D00, this component contains a large fraction of the baryons ($\sim 30\%$ by mass are in this WHIM, with temperatures between $10^5$ and $10^7$ K).

In our model, much of the very soft XRB is produced by this diffuse WHIM gas, rather than by galaxy groups and halos. We have calculated the mean intensity in our simulations in a band centered around 0.25 keV, and found it to be 13 keV s$^{-1}$ cm$^{-2}$ sr$^{-1}$keV$^{-1}$. Observationally, different analyses (Cui et al. 1996, Wang & Ye 1996, Warwick & Roberts 1998) find that after subtracting the AGN contribution in the very soft X-rays, at most $\sim 4-15$ keV s$^{-1}$ cm$^{-2}$ sr$^{-1}$keV$^{-1}$ can be in an IGM component. This is fairly close to our simulation predictions, although probably a bit lower.

Several authors have recently argued that supernova feedback of about 1 keV per baryon is required to prevent the gas in galaxy halos and groups from over-producing the diffuse soft XRB. Pen (1999) reached an estimate of 230 keV s$^{-1}$ cm$^{-2}$ sr$^{-1}$keV$^{-1}$ at 0.25 keV, using a hydrodynamical simulation without cooling and assuming all the baryons were gaseous with an emission-weighted temperature of $1.5 \times 10^6$ K, typical of galactic halos. Wu, Fabian, & Nulsen (1999) used a semi-analytic model to estimate a background of 35 to 60 keV s$^{-1}$ cm$^{-2}$ sr$^{-1}$keV$^{-1}$ at 0.25 keV, in the absence of supernova feedback. This calculation allowed the gas temperature to vary as a function of group circular velocity, an improvement on the Pen (1999) calculation; the resulting background was dominated by groups of galaxies.

Our simulations, by contrast, demonstrate that extreme supernova feedback is not required to match the observed intensity of 0.25 keV emission. There are several reasons why our conclusions differ from those of Pen and Wu et al. (see also the discussion in Davé et al. 2000). First, as mentioned above, only 30% of the gas is in the WHIM. As Bryan (2000) also points out, the efficiency of forming galaxies is higher in groups than in clusters, which removes much of the gas in these lower mass systems. The papers cited above assumed that essentially all of the baryons in any virialized halo were in a hot X-ray emitting medium. Second, the gas in these papers is assumed to be isothermal in the potential of a cuspy dark matter halo, so that most of the emission is radiated at the center of the halo. In our simulation, we find instead that the X-ray-emitting gas typically has a core with a radius of several hundred kpc (see Figure 7 of Davé et al. 2000, which is based on this simulation). The strong emission at the center is thus eliminated. This core may be somewhat influenced by our numerical resolution, but the analytic model by Bryan (2000) also finds such a core. Third, in our simulations much of the energy released in gravitational clustering emerges in the form of atomic lines, principally Ly$\alpha$, rather than in X-rays (Fardal et al. 2000). As our XRB predictions are slightly higher than the observational limits, it is possible that a modest increase of feedback in the simulations would improve the agreement. We will report on a study of the X-ray luminosity function of galaxy groups, which are most sensitive to feedback effects, in future work.

On the observational side, maps of extragalactic soft X-ray emission are extremely difficult to make, mainly because of emission and absorption by our galaxy. The ROSAT All Sky Survey is dominated by galactic thermal emission over much of the sky, and even in regions close to the galactic poles, there is uncertainty in the contribution of this component to the measured X-ray fluctuations (see, e.g., Soltan et al. 1996). It is possible that realistic theoretical maps such as those we have presented here can play a role in testing the procedures used to remove galactic foreground contamination, just as they do in the study of the Cosmic Microwave Background (e.g., Bouchet & Gispert 1999).

Ultimately, one can hope to study cosmology with the small scale structure of the XRB. The contribution from various species of AGN is certainly complicated, but because the AGN emission is widely spread in redshift, the clustering of the soft XRB seems to be dominated (at least in the model we have studied) by the IGM. The physical processes involved in the emission are relatively simple, although the question of feedback and the effect it will have on small scale structure must be studied. The new X-ray satellites, *Chandra* and *XMM-Newton*, should soon measure clustering accurately on the scales for which we have made predictions in this paper. Among the many further analyses that can be made are cross-correlations of the XRB with Sunyaev-Zel'dovich and weak-lensing maps, as well as measuring the cross-correlation with galaxies as function of redshift. We also hope that simulated skymaps such as ours will help advance methods for detecting emission from the WHIM and thus help to complete the census of local baryons.

We thank Volker Springel, Chris Metzler and Max Tegmark for useful discussions. This work was supported by NASA Astrophysical Theory Grants NAG5-3820, NAG5-3922, and NAG5-3111, by NASA Long-Term Space Astrophysics Grant NAG5-3525, and by the NSF under grants ASC93-18185, ACI96-19019, and AST-9802568. TDM is supported by NASA through Chandra Fellowship grant number PF8-10005 awarded by the Chandra Science Center, which is operated by the Smithsonian Astrophysical Observatory for NASA under contract NAS8-39073. The simulations were performed at the San Diego Supercomputer Center, NCSA, and the NASA/Ames Research Center.

REFERENCES

Aguirre, A., Hernquist, L., Weinberg, D. H., Katz, N., & Gardner, J., 2000, ApJ, submitted, astro-ph/0006345
Aguirre, A., Hernquist, L., Katz, N., Gardner, J. & Weinberg, D. H., 2000, ApJ, submitted, astro-ph/0006346
Blanchard, A., Wachter, K., Evrard, A. E., & Silk, J., 1992, ApJ, 391, 1
Bryan, G., 2000, ApJL, accepted, astro-ph/0009286
Bouchet, F. R., & Gispert, R., 1999, New Ast, 4, 443
Boyle, B. J., Georgantopoulos, I., Blair, A. J., Stewart, G. C., Griffiths, R. E., Shanks, T., Gunn, K. F., Almaini, O., 1998, MNRAS, 296, 1
Brandt, W. N., Hornschemeier, A. E., Schneider, D. P., Garmire, G. P., Chartas, G., Hill, Gary J., MacQueen, P. J., Townsley, L. K., Burrows, D. N., Koch, T. S., Nousek, J. A., Ramsey, L. W., 2000, AJ, 119, 2349
Bryan, G., & Norman, M. L., 1998, ApJ, 495, 80
Burles, S., & Tytler, D., 1998, ApJ, 499, 699
Cattaneo, A., 1999, MNRAS, submitted, astro-ph/9907335
Cattaneo, A., Haehnelt, M. G., Rees, M. J., 1999, 308, 77 (**CHR**)
Cen, R., Kang, H., Ostriker, J. P., & Ryu, D., 1995, ApJ, 451, 436
Cen, R. & Ostriker, J. P. 1999, ApJ, 519, L109
Croft, R. A. C., & Metzler, C. M. 2000, ApJ, in press, astro-ph/0005384
Cui, W., Sanders, W. T., McCammon, D., Snowden, S., & Womble, D. S., 1996, ApJ, 117
da Silva, A. C., Barbosa, D., Liddle, A. R., Thomas, P. A., MNRAS, 317, 37
Davé, R., Dubinski, J., & Hernquist, L. 1997, NewAst, 2, 71
Davé, R., Hernquist, L., Katz, N. & Weinberg, D. H., 1999a, ApJ, 511, 521
Davé, R., Gardner, J. P., Hernquist, L., Katz, N. & Weinberg, D. H., 1999b, Proceedings of Les Rencontres Internationales de l'IGRAP, Clustering at High Redshift, Marseille, astro-ph/9910221
Davé, R., Cen, R., Ostriker, J. P., Bryan, G., Norman, M. L., Hernquist, L., Katz, N., Weinberg, D. H., O'Shea, B., 2000, ApJ, submitted, astro-ph/0007217 (**D00**)
Davé, Katz, N., Weinberg, D. H., & Hernquist, L. 2001, ApJ, submitted
de Lapparent, V., Geller, M. J. & Huchra, J. P., 1986, ApJ, 302, L1
Elvis, Martin, Wilkes, Belinda J., McDowell, Jonathan C., Green, Richard F., Bechtold, Jill, Willner, S. P., Oey, M. S., Polomski, Elisha, Cutri, Roc, ApJS, 95, 1
Fardal, M. A., Katz, N., Gardner, J. P., Hernquist, L., Weinberg, & Davé, R. 2000, ApJ, accepted, astro-ph/0007205
Ferrarese, L., Merritt, D., 2000, ApJ, 539, 9
Frenk, C. S., White, S. D. M., Bode, P., Bond, J. R., Bryan, G. L., Cen, R., Couchman, H. M. P., Evrard, A. E., Gnedin, N., Jenkins, A., Khokhlov, A. M., Klypin, A., Navarro, J. F., Norman, M. L., Ostriker, J. P., Owen, J. M., Pearce, F. R., Pen, U.-L., Steinmetz, M., Thomas, P. A., Villumsen, J. V., Wadsley, J. W., Warren, M. S., Xu, G.,& Yepes, G., 1999, ApJ, 525, 554
Fukugita, M., Hogan, C. J., Peebles, P. J. E., 1998 ApJ, 503, 518
Gebhardt, K., Bender, R., Bower, G., Dressler, A., Faber, S. M., Filippenko, A. V., Green, R., Grillmair, C., Ho, L. C., Kormendy, J., Lauer, T. R., Magorrian, J., Pinkney, J., Richstone, D., Tremaine, S., 2000, ApJ, 539L, 13
Governato, F., Moore, B., Cen, R., Stadel, J., Lake, G., Quinn, T., 1997, New Ast, 2, 91
Hasinger, G., Burg, R., Giacconi, R., Schmidt, M., Trümper, J., & Zamorani, G., 1998, A&A, 329, 495
Hellsten, U., Gnedin, N. Y., Miralda-Escudé, J., 1998, ApJ, 509, 56
Hernquist, L. & Katz, N. 1989, ApJS, 70, 419
Kaiser, N., 1991, ApJ, 383, 104
Katz, N. & White, S. D. M., 1993, ApJ, 412, 455
Katz, N., Weinberg D.H., & Hernquist, L. 1996, ApJS, 105,
Kauffmann, G., & Haehnelt, M., 2000, MNRAS, 311, 576 (**KH**)
Lewis, G. F., Babul, A., Katz, N., Quinn, T., Hernquist, L., & Weinberg, D. H., 2000, ApJ, 536, 623
Magorrian, J., Tremaine, S., Richstone, D., Bender, R., Bower, G., Dressler, A., Faber, S. M., Gebhardt, K., Green, R., Grillmair, C.; Kormendy, J., Lauer, T., 1998, AJ, 115, 2285
Marshall, F. et al. 1980, AJ, 235, 4
Merritt, D, Cruz, F., & Milosavljevic, M., 2000, in "Dynamics of Star Clusters and the Milky Way," eds. S. Deiters et al. , ASP Conf. Series, astro-ph/0008497
Metzler, C., & Evrard, A. E., 1994, ApJ, 437, 564
Mushotzky, R. F., Cowie, L. L., Barger, A. J., & Arnaud, K. A., 2000, Nature, 404, 459
Pearce, F. R., Jenkins, A., Frenk, C. S., Colberg, J. M., White, S. D. M., Thomas, P. A., Couchman, H. M. P., Peacock, J. A., Efstathiou, G., 1999, ApJ, 521
Pen, U.-L., 1999a, ApJ, 510, L1
Pen, U.-L., 1999b, ApJS, 120, 49
Perna, R., & Loeb, A., R., 1998, ApJ, 503, 35L
Pierre, M., Bryan, G., Gastaud, R., 2000, A&A, 356, 403
Raymond, J. C., & Smith, B. W., 1977, ApJS, 35, 419
Ritchie, B. W., & Thomas, P. A., 2000, MNRAS, submitted, astro-ph/0005357
Scharf, C., Donahue, M., Voit, G. M., Rosati, P., Postman, M., 2000, ApJ, 528, L73
Schmidt, M., Hasinger, G., Gunn, J., Schneider, D., Burg, R., Giacconi, R., Lehmann, I., MacKenty, J., Trümper, J., & Zamorani, G. 1998, A&A, 329, 495
Soltan, A. M., Hasinger, G., Egger, R., Snowden, S., Trümper, J., 1996, A&A, 305, 17
Soltan, A. M., Hasinger, G., Egger, R., Snowden, S., Trümper, J., 1997, A&A, 320, 705
Soltan, A. M., Freyberg, M., Hasinger, G., Miyaji, T., Treyer, M., Trümper, J., 1999, A&A, 349, 354
Seljak, U., Burwell, J. & Pen, U.-L., 2000, PRD, submitted, astro-ph/0001120
Springel, V., White, M. & Hernquist, L., 2000, ApJ, submitted, astro-ph/0008133
Tsai, J. C., Katz, N. & Bertschinger, E., 1994, ApJ 423, 553.
Wang, Q. D., & Ye, T. 1996, NewAst, 1, 245
Warwick, R. S., & Roberts, T. P., 1998, Astronomische Nachrichten, 319, 59
White, M., & Hu, W., 2000, ApJ, 537, 1
Wilman, R. J., Fabian, A. C., Nulsen, P. E. J., MNRAS, in press, astro-ph/0008019
Weinberg, D. H., Davé, R., Gardner, J. P., Hernquist, L., & Katz, N., 1999, In "Photometric Redshifts and High Redshift Galaxies", eds. Weymann, R., Storrie-Lombardi, L., Sawicki M., & Brunner, R. (San Francisco: ASP Conference Series), astro-ph/9908133
Wu, K. K. S., Fabian, A. C., & Nulsen, P. E. J., MNRAS, submitted, astro-ph/9910122

## APPENDIX

## ALLOWING FOR A TWO-PHASE MEDIUM

### *Introduction*

The simulation includes the cooling processes that transform collapsing dense gas into cold galactic clumps that can then form stars. This galactic gas is often in close proximity to intracluster gas, which is in a completely different phase, at least $\sim 100$ times less dense and $\sim 100$ times hotter or more. The SPH density estimate we use (Hernquist & Katz 1989) is evaluated from the positions of the 32 nearest neighbours of each particle, regardless of their temperature. With very high mass resolution, there should be no problems with resolving the distinct gas phases. However, in practice we have a limited number of particles, so that the standard density estimate for some hot intracluster gas that is close to galaxies will include cold, much denser particles, which are in a different phase. This results in a spuriously high density estimate for these hot particles, something that is especially problematic when calculating their X-ray emission. For our present purposes, this problem can be easily mitigated by

separating the hot and cold dense gas phases before evaluating the density, after the simulation has been run. In the same way that the baryonic material in star particles does not contribute to gas particle density estimates, we remove the cold, collapsed gas from the calculation of the density of hot gas.

In this Appendix we will illustrate the effect of this correction on the X-ray luminosities of particles, and test that it is robust by varying the thresholds we use for excluding particles. We will also carry out a simple test involving an isothermal sphere with a cold gas clump at the center to show that the effect can be reproduced in a controlled situation. Finally, we compare the X-ray luminosity of a galaxy group in a smaller, higher mass resolution simulation to similar groups in our large simulation, to check that separating the gas phases has the expected smaller effect on the X-ray luminosity at higher resolution.

We note that different solutions for dealing with the effect of two gas phases on galaxy formation in SPH simulations have been proposed by Pearce et al. (1999), and Ritchie & Thomas (2000). A detailed study of the effect on galaxies should be carried out by running simulations with a different method for estimating the density (e.g., a direct solution of the continuity equation [V. Springel, private communication]), and is beyond the scope of this paper.

*Two-phase density estimates*

We recalculate the density estimates for hot particles in the simulation by excluding cold, dense particles from the kernel estimation. We define hot particles to be those with $T > 10^5$K and set the threshold for exclusion to be $T < 10^{4.5}$K and $\rho > 1000$. The effect of varying these thresholds is negligible (see below).

In Figure A14 we show the positions and soft-band X-ray luminosities of some particles before and after the density correction. The panels are centered on the particle with the highest uncorrected X-ray luminosity ($7 \times 10^{42}$ erg s$^{-1}$), which resides in a group with a circular velocity of 500 km s$^{-1}$. Clumps of cold particles are embedded in the intragroup gas, which, if included in the density estimate of the hot particles, leads to the artificially high X-ray emission seen in Figure A14b. After the correction, the X-ray luminosities of the particles near the galaxy are similar to those in the rest of the intragroup medium. The corrected soft-band luminosity of the group is $1.8 \times 10^{42}$ erg s$^{-1}$, a factor 12 lower than the uncorrected value.

With our fiducial parameters for excluding cold gas, we find that the average volume emissivity of the whole simulation volume is $1.55 \times 10^{-35}$ erg s$^{-1}$ cm$^{-3}$, and $7.01 \times 10^{-36}$ erg s$^{-1}$ cm$^{-3}$, for the $0.5-2$ keV and $2-10$ keV bands, respectively. This is a factor of [13,7] smaller than with the uncorrected density estimate, for the [soft,hard] band. As a test that this correction is robust, we raise the cold density limit to $\rho > 10^5$, and find $1.60 \times 10^{-35}$ erg s$^{-1}$ cm$^{-3}$, $7.11 \times 10^{-36}$ erg s$^{-1}$ cm$^{-3}$ (for $0.5-2$, $2-10$ keV emissivities). If we only change densities for hot gas if the hot gas ($T > 10^5 K$) density was previously $> 100$, we find (with cold $\rho$ limit of 1000) $1.55 \times 10^{-35}$ erg s$^{-1}$ cm$^{-3}$, $7.07 \times 10^{-36}$ erg s$^{-1}$ cm$^{-3}$ (for $0.5-2$, $2-10$ keV).

These large changes in the thresholds for including cold particles and recalculating the densities of hot particles change the corrected X-ray emission by 3% or less. This is a good indication that our correction is sensible. This recalculation of the density radically affects a small number of particles but has virtually no effect on the rest. In the plot of temperature against density (Figure 1) we used

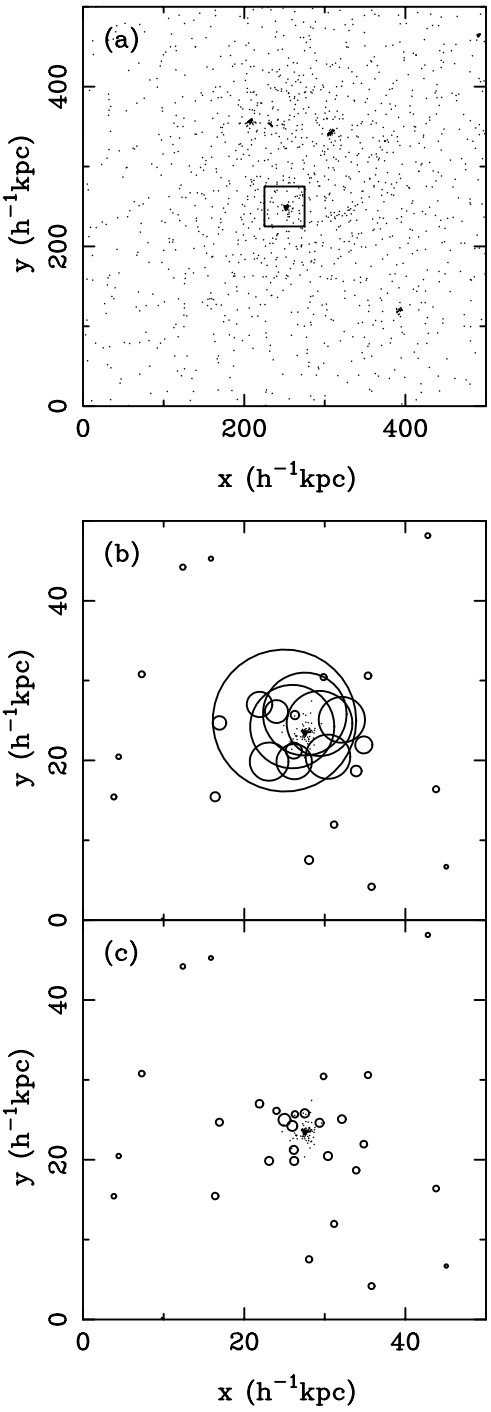


FIG. A14.— (a) A plot of particle positions in a $500h^{-1}$kpc cube centered on the particle with the highest X-ray luminosity in the simulation. (b) The central $50h^{-1}$kpc wide volume shown in the previous panel. We plot each particle using a circle of area proportional to its X-ray luminosity. (c) The same as panel (b), except that we have corrected the density estimates by separating the hot and cold gas into two phases before calculating the X-ray luminosities.

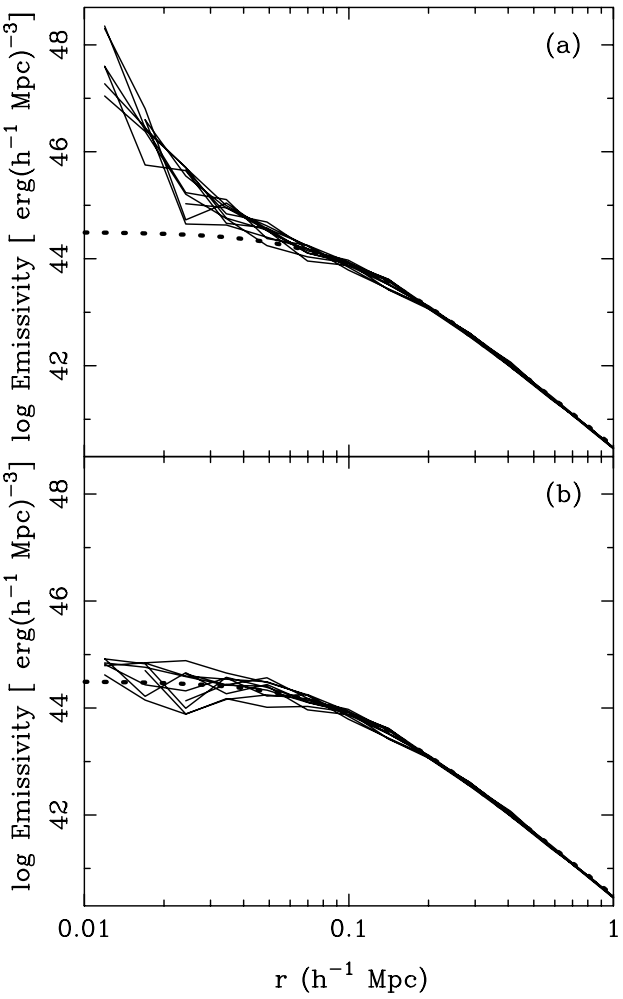


FIG. A15.— Solid lines: X-ray emission from isothermal spheres with an embedded central galaxy: (a) Using the standard SPH density estimation, and (b) after excluding cold particles from the density estimate of hot particles. The dashed line shows the correct analytic result.

the corrected densities, as well as in the results in the main text of the paper.

*Isothermal sphere test*

As an additional test of our correction, we set up a static toy model of a group. This is to demonstrate that the spurious X-ray emission in the simulation can be reproduced, and is simply due to the density kernel estimation, something that can be tested without hydrodynamics.

We distribute 10,000 particles by randomly sampling the density profile

$$\rho(r) \propto \frac{1}{r^2 + r_c^2}, \tag{A1}$$

to approximate an isothermal sphere with a core. The parameter $r_c$ is set to $100h^{-1}$kpc, and the temperature of the particles to $10^7$ K. We add a top hat sphere of radius $10h^{-1}$kpc containing 2500 particles to the center of the group. These particles have a temperature of $10^4$ K and represent a galaxy. We make sure that no hot intragroup particles lie within the galaxy radius.

The X-ray emissivity profiles of 10 such toy groups set up using different random seeds are shown in the top panel of Figure A15, along with the analytic profile. We can see that as we approach the central galaxy, the emission rises rapidly above the correct result, due to the hot particles near the center having their densities overestimated. The total average luminosity of the groups is $1.1 \times 10^{43}$ erg s$^{-1}$, and there is a wide spread in individual values, with some having luminosities a quarter of the mean, and some twice the mean.

If we do not include the galactic gas in the hot gas density estimate, as would happen with our correction, the analytic profile is well reproduced (Figure A15b). The corrected mean luminosity is $2.9 \times 10^{42}$ erg s$^{-1}$, with a maximum 10% variation between groups, due to shot noise. We note that the difference between the uncorrected and corrected luminosities (a factor $\sim 4$) is lower than that for the simulation group in Figure A14. This is presumably due to the fact that there is more than one galaxy in the simulation group.

*Simulation resolution test*

With higher mass resolution, we would resolve the two distinct gas phases better, so that the correction to the X-ray luminosities that occurs when we separate them by hand should be smaller. Exploring the dependence of the correction on resolution is therefore another way of checking its validity.

Although we cannot resimulate our entire volume at higher resolution, a simulation in a much smaller box is available, one that was also used by D00. The cosmological model parameters are identical to our 50 $h^{-1}$Mpc ΛCDM simulation, but the box side-length is 11.11 $h^{-1}$Mpc, which gives a particle gas mass that is 8 times smaller, $1.1 \times 10^8 M_\odot$. The linear force resolution is also twice as high.

To compare like with like, we do not consider the mean total emission from the box (which in the smaller volume is affected strongly by missing large-scale power), but compare galaxy groups of similar size taken from the two simulations. We have picked out groups using a standard friends-of-friends algorithm on the gas and dark matter particle distributions. The circular velocity at the virial radius, $V_c$, was estimated using a spherical overdensity criterion. In Figure A16, we plot the soft-band X-ray luminosities (we refer to the soft-band for the rest of this subsection) of these groups against $V_c$, for both the original and corrected density estimates.

We concentrate on the largest group in the 11.11 $h^{-1}$Mpc simulation (with $V_c = 410$ km s$^{-1}$), because it is responsible for 74% of the (corrected) X-ray emission. Groups with this value of $V_c$ and higher account for 78% of the X-ray emission in the large box, so that tests carried out on such groups will be representative of the total X-ray luminosity. From Figure A16a we can see that the high-resolution group has a luminosity less than the other groups with similar $V_c$. The 34 groups in the large simulation with $V_c$ within 10% of 410 km s$^{-1}$ have a mean uncorrected luminosity of $1.0 \times 10^{43}$ erg s$^{-1}$, which is 6 times higher than that of the high-resolution group. After the two phases have been separated (Figure A16b), the mean luminosity of the low resolution groups falls by a factor of 15, compared to 3 for the high resolution group. The latter is now on the high end, with luminosity some 75% higher than the mean.

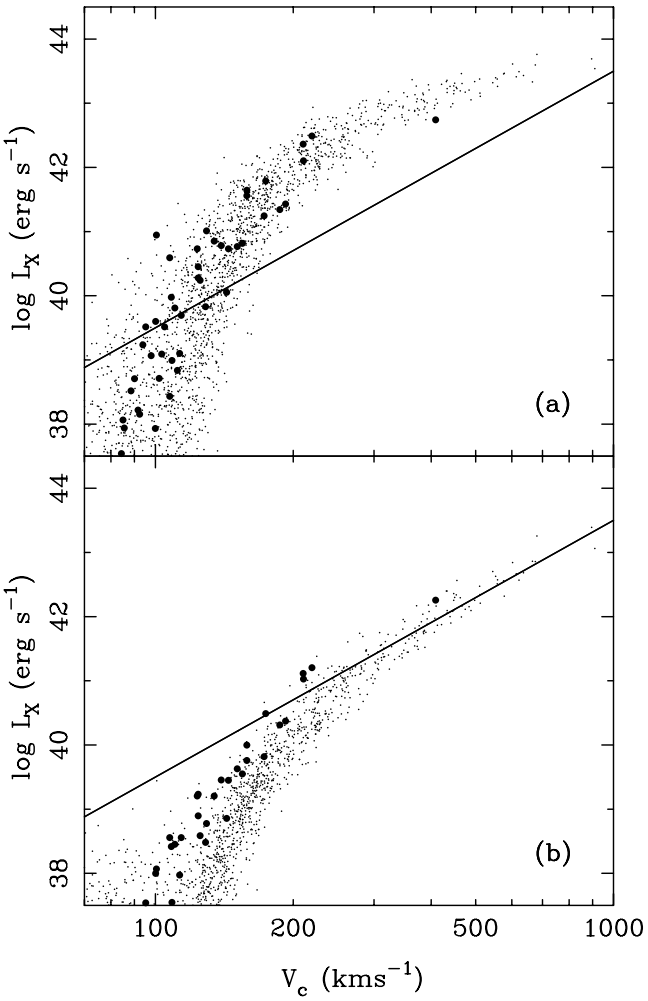


FIG. A16.— The soft band X-ray luminosities of groups plotted against their circular velocities, for two simulations with different mass resolutions. The dots represent groups in the large simulation we have used in the main body of the paper, and the large points groups taken from a much smaller box with 8 times higher mass resolution (see text). In panel (a) we show the uncorrected luminosities, and (b) the corrected luminosities that result when we separate the cold dense phase from the hot gas. The line $L_X \propto V_c^4$ is plotted with the same (arbitrary) amplitude in each panel, to act as a reference line.

With higher resolution, we find that the correction due to considering the two gas phases separately is smaller, as one would expect. We would like more high resolution large groups, to make a good statistical comparison, but this is not possible. For the moment we can look at the small groups, with $V_c \sim 200$ km s$^{-1}$ and less. From Figure A16 we can see that they have much larger correction factors than the large groups, and that the higher resolution groups again have smaller corrections. The high-resolution groups are also on average 3 times more luminous than the others, although as only $< 5\%$ of the total luminosity comes from groups below $V_c \sim 200$ km s$^{-1}$, this is not significant for the total emission.

Another point of note is that the dispersion about the mean luminosity for a given $V_c$ is noticeably smaller for the corrected values. This is because the spurious luminosities are affected by discreteness noise, being due to only a few particles, as we have seen in the previous subsection.

The main aim of this resolution test was to see whether the two-phase density correction has a smaller effect at higher resolution. However, we would obviously also like to study how the mean X-ray emissivity of the simulation volume is affected by resolution. We have found that the smallest groups, which contribute only a few percent to the total, are affected by resolution (as stated above, a factor 3 higher luminosity for a mass resolution 8 times better). Considering material more representative of the bulk of the emission, the one large group at high resolution has 75% higher luminosity than the low resolution mean. It seems plausible that the difference may be even smaller for larger groups and clusters. Even if this is not the case, it does not seem that the X-ray background intensity will be more than mildly resolution dependent. This is what might be expected if much of the soft X-ray emitting material is in relatively diffuse gas, rather than being tightly bound to a hierarchy of small objects.

*Summary*

In this Appendix we have shown that because of the way the SPH densities are estimated, we need to be careful with our treatment of hot X-ray emitting gas in close proximity to cold dense gas. With limited mass resolution, the densities of a small number of hot particles are overestimated, something which has been realized in simulations of galaxy formation (Pearce et al. 1999; Ritchie & Thomas 2000), and which is especially important for the study of X-ray emission. The simple solution to the problem is to separate the gas phases before estimating the density and the X-ray emissivity. We have done this, and carried out a number of tests to check that the procedure is both reasonable and robust. First, we have shown that the mean corrected X-ray emissivity varies by $< 3\%$ when the density and temperature thresholds for separating the phases are varied by a factor of 100. Second, we have shown that the effect of two phases on the X-ray emission can be reproduced and corrected in a controlled situation, an isothermal sphere. Third, we have found that with higher mass resolution, the correction factor is smaller, as we would expect. Effects such as these are probably responsible for the steep central X-ray profiles seen in simulations of galaxy clusters that have included cooling (e.g. Katz & White 1993; Tsai, Katz & Bertschinger 1994; Lewis et al. 2000). Using the corrected densities in the calculation of the X-ray emissivities may well bring these central regions into agreement with observations.